RMetS
Royal Meteorological Society

Ocean ensemble forecasting. Part I: Ensemble Mediterranean winds from a Bayesian hierarchical model

Ralph F. Milliff,[a]* Alessandro Bonazzi,[b] Christopher K. Wikle,[c] Nadia Pinardi[b] and L. Mark Berliner[d]

[a]*NWRA, Colorado Research Associates Div., Boulder, CO, USA*
[b]*Operational Oceanography Group, INGV, Bologna, Italy*
[c]*Statistics Department, University of Missouri, Columbia, MO, USA*
[d]*Statistics Department, Ohio State University, Columbus, OH, USA*
*Correspondence to: R. F. Milliff, 3380 Mitchell Lane, Boulder, CO 80301, USA. E-mail: milliff@cora.nwra.com

A Bayesian hierarchical model (BHM) is developed to estimate surface vector wind (SVW) fields and associated uncertainties over the Mediterranean Sea. The BHM–SVW incorporates data-stage inputs from analyses and forecasts of the European Centre for Medium-Range Weather Forecasts (ECMWF) and SVW retrievals from the QuikSCAT data record. The process-model stage of the BHM–SVW is based on a Rayleigh friction equation model for surface winds. Dynamical interpretations of posterior distributions of the BHM–SVW parameters are discussed. Ten realizations from the posterior distribution of the BHM–SVW are used to force the data-assimilation step of an experimental ensemble ocean forecast system for the Mediterranean Sea in order to create a set of ensemble initial conditions. The sequential data-assimilation method of the Mediterranean forecast system (MFS) is adapted to the ensemble implementation. Analyses of sample ensemble initial conditions for a single data-assimilation period in MFS are presented to demonstrate the multivariate impact of the BHM–SVW ensemble generation methodology. Ensemble initial-condition spread is quantified by computing standard deviations of ocean state variable fields over the ten ensemble members. The methodological findings in this article are of two kinds. From the perspective of statistical modelling, the process-model development is more closely related to physical balances than in previous work with models for the SVW. From the ocean forecast perspective, the generation of ocean ensemble initial conditions via BHM is shown to be practical for operational implementation in an ensemble ocean forecast system. Phenomenologically, ensemble spread generated via BHM–SVW occurs on ocean mesoscale time- and space-scales, in close association with strong synoptic-scale wind-forcing events. A companion article describes the impacts of the BHM–SVW ensemble method on the ocean forecast in comparisons with more traditional ensemble methods. Copyright © 2011 Royal Meteorological Society

Key Words: QuikSCAT surface winds; ECMWF analysis winds; physics-based priors

Received 13 November 2009; Revised 15 September 2010; Accepted 7 December 2010; Published online in Wiley Online Library 3 May 2011

Citation: Milliff RF, Bonazzi A, Wikle CK, Pinardi N Berliner LM. 2011. Ocean ensemble forecasting. Part I: Ensemble Mediterranean winds from a Bayesian hierarchical model. *Q. J. R. Meteorol. Soc.* **137**: 858–878. DOI:10.1002/qj.767

1. Introduction

The Mediterranean Forecast System (MFS) is an operational ocean forecasting service, providing 10 day forecasts for the state of the Mediterranean Sea every day* (Pinardi *et al.*, 2003). As for any modern forecasting system, MFS scientists are interested in using ensemble ocean forecasts to estimate the space–time properties of forecast uncertainties in order better to understand predictability issues and to add value for forecast user applications. In this article we describe a practical means for generating ocean ensemble initial conditions and driving ocean ensemble forecasts, with realizations from a posterior distribution of the surface vector winds (SVWs) as obtained from a Bayesian hierarchical model (BHM). The BHM–SVW in the MFS ensemble forecast setting is an implementation on a large scale (i.e. in terms of degrees of freedom), with significant emphasis on efficiency (i.e. as driven by the ocean forecast-cycle constraints). As such, the article delves into the details of BHM design and implementation. The article ends with a description of multivariate ensemble initial-condition spread as driven by the BHM–SVW for MFS over one data-assimilation cycle. A companion article (Bonazzi *et al.*, 2010, hereinafter Part 2) compares the impacts on the MFS forecasts of the BHM–SVW ensemble generation method versus more traditional methods over many assimilation and forecast cycles.

A variety of methods for global ensemble weather forecasts have been developed since the late 1980s, and have been in operational use since the 1990s (see e.g. the comprehensive review by Ehrendorfer (2007) and review articles focusing on ensemble Kalman filter methods (Evensen, 2003; Ehrendorfer, 2008)). As in initial-condition generation methods for the global atmosphere, computational efficiencies are critical for the practical application of any new methodology for ensemble generation in ocean forecasting. The initial-condition ensemble spread for ocean forecast systems must be optimized over affordable ensemble sizes, e.g. $\mathcal{O}(10)$ members. Also, ocean ensemble initial conditions should be in dynamical and thermodynamical balance so that the initial forecast time steps are not dominated by artificial adjustments toward balance.

However, the regional ocean forecast system perspective differs from that of the atmosphere, and so the ensemble initial-condition generation methodology will differ as well. Forecast time-scales for the ocean ($\mathcal{O}$(days)) are longer than those for the atmosphere ($\mathcal{O}$(hours)) because of different time-scales for hydrodynamic instabilities in the two fluids (McWilliams *et al.*, 1983; Pinardi and Robinson, 1987). Ocean forecast-error amplification is most often related to slower adiabatic processes (e.g. baroclinic instabilities), while faster diabatic processes (e.g. convective instabilities) are associated with the largest error growth in atmospheric forecasts. Ocean ensemble forecast system design considerations, including ensemble initial-condition generation methods, should therefore be adapted to longer time-scales for error growth, with accurate representations of, and estimates of uncertainties for, adiabatic processes in the upper ocean.

Operational ocean forecast systems such as MFS focus on sea-surface and upper-ocean fields of currents, temperature and salinity, as well as vertically integrated properties of the upper ocean including upper-ocean heat content, dynamic topography, etc. Ensemble initial-condition generation methods should produce a realistic spread in these fields. Moreover, the initial-condition spread will be most useful if it occurs at locations and on spatial scales that are particularly uncertain in the ocean forecast system at any given time, i.e. for any given forecast cycle.

The SVW drives momentum inputs to the upper ocean, and surface wind speed modulates transfers of heat and material properties (i.e. fresh water) at the air–sea interface. Ocean heat losses at the air–sea interface drive water-mass formation processes. Surface shear induces barotropic and baroclinic instabilities. Combinations of these processes are responsible for the broad-band spectrum of ocean currents and eddies throughout the world ocean (Weijer and Gille, 2005; Kersale *et al.*, 2010). Simple, physically based models of the SVW over the ocean consider balances between terms including the effects of surface pressure gradients, Coriolis acceleration and surface friction (Stevens *et al.*, 2002). Ocean dynamical and thermodynamical adjustment to surface wind variability on horizontal scales that characterize the MFS ocean forecast output (i.e. $\mathcal{O}$(10 km)) occurs at ocean mesoscales (POEM Group, 1992; Pinardi and Masetti, 2000 and references therein). From an ensemble forecasting perspective, the SVW field provides a means of perturbing the ocean fields of interest in dynamically and thermodynamically consistent ways.

From observational and modelling viewpoints, the ocean SVW on the scale of MFS interest is relatively well known. While accurate surface wind observations from *in situ* point sources (i.e. moorings, drifters, etc.) are relatively rare (Nittis *et al.*, 2007; Ruti *et al.*, 2008), the technology of retrieving SVW fields in swathes from space-borne scatterometer systems is now highly refined (for background see Freilich, 1996 ATBD). Moreover, the properties of the observational error in SVW retrievals from scatterometer data are also well-known (Freilich, 1997; Ebuchi *et al.*, 2002; Draper and Long, 2002; Portabella and Stoffelen, 2002; Freilich and Vanhoff, 2003).

The BHM to be developed here exploits physically based models, observations and well-characterized error properties of the SVW to obtain posterior distributions for the winds over the Mediterranean Sea every 6 h at 0.5° resolution. These BHM–SVW posterior distributions form the basis of a new ocean ensemble forecast (OEF) method. Realizations from the posterior distribution for the surface wind are used to (1) drive an ensemble of 14 day sequential data assimilation cycles over the analysis period (days 1*A*–14*A*) and (2) drive 10 day ensemble ocean forecasts (days 1*F*–10*F*). The ensemble ocean initial conditions are obtained at the end of the analysis period (day 14*A*, 1200 UTC) and one ocean forecast is launched from each initial-condition ensemble member. In this article we describe the construction of the BHM, examine posterior distributions for parameters of the BHM–SVW and demonstrate the BHM–SVW impact on the ensemble ocean initial conditions for a single data-assimilation cycle. Part 2 compares the impact of the OEF based on BHM–SVW forcing with OEF impacts based on more traditional approaches over many ocean forecast cycles.

*See http://gnoo.bo.ingv.it/mfs. See also the MFSTEP special issue, *Ocean Sciences*, 2007.

The number and scope of applications of BHM in atmosphere–ocean science are increasing (Berliner, 2003; Berliner *et al.*, 2003; Wikle, 2003; Fox and Wikle, 2005; Anderson *et al.*, 2007; Song *et al.*, 2007; Berliner and Kim, 2008). Details of each BHM implementation are important in assessing the implications of the derived posterior distributions. We focus on details of the BHM–SVW development here in data-stage inputs; process-model development and error models to express uncertainty. While it is particularly appropriate for the ocean forecasting application, pertubing forcing fields to generate a realistic spread in model initial-condition forecasts embodies an approach with broader implications (e.g. climate reconstructions from uncertain historical forcing datasets). The detailed description of the BHM–SVW development here therefore provides a blueprint for BHM applications in other areas as well.

Background information is provided in the next section, regarding (1) properties of SVW fields from QuikSCAT observations and ECMWF analyses, (2) the record of SVW BHMs using scatterometer data and (3) specifics of MFS data-assimilation methods relevant to the development of ensemble ocean initial conditions. The components of the BHM–SVW for ensemble ocean forecasting in MFS are developed in section 3. BHM–SVW results are examined in section 4. Section 5 provides a discussion of dynamical interpretation and validation of the BHM–SVW posterior distribution. Samples of ensemble ocean initial conditions driven by BHM–SVW for a single assimilation period are also presented in section 5. Conclusions are drawn in section 6. Appendix A provides the BHM–SVW derivation and the full conditional expressions that are sampled in a Markov chain Monte Carlo (MCMC) algorithm to estimate realizations of the posterior distribution for SVW in the Mediterranean Sea. Hyperprior specifications for the BHM–SVW are listed in Appendix B.

2. Background

2.1. SVW from ECMWF analyses and QuikSCAT observations

The BHM implemented here makes use of SVW datasets from ECMWF analyses and SVW retrievals from QuikSCAT observations. Figure 1 depicts typical Mediterranean Sea coverage for ECMWF analyses (red) and QuikSCAT SVW retrievals (black) for a 24 h period (2 February 2005). The ECMWF analyses are available four times daily: at midnight, 0600, noon and 1800 UTC. The ECMWF surface data utilized by MFS occur on a regular 0.5° resolution grid that spans the Mediterranean Sea domain (Figure 1).[†] In contrast, SVWs are retrieved in 25 km resolution wind-vector cells (WVC) within the QuikSCAT [‡] swathes over the ocean, as shown in Figure 1. QuikSCAT was in a polar-orbit orientation with an 8° declination, such that ascending swathes occurred in the Mediterranean in the morning hours inclined from southeast–northwest (panel 2 in Figure 1). Swathes in descending branches of the polar orbit crossed the Mediterranean in the evening hours from northeast–southwest (panel 4 in Figure 1). The SVW retrievals in Figure 1 overlay the ECMWF analyses nearest in time to the QuikSCAT overflight. The time between consecutive QuikSCAT orbits was about 100 min. The maximum temporal difference between ECMWF analyses and QuikSCAT SVW retrievals in each panel is 3 h. Inconsistencies that might arise from the temporal mismatch in data availability are encompassed in the prescriptions of dataset uncertainties that are described below.

The width of the QuikSCAT swathe over which useful SVW can be retrieved is about 1600 km. Reliable SVW cannot be retrieved at the extreme edges of the swathe (not shown in Figure 1) or from QuikSCAT observations in instances of heavy rain. Rain-contaminated WVC are flagged in the QuikSCAT science data product of the NASA Jet Propulsion Laboratory used here.[§] The swathe locations precess westward, with exact repeats every 4 days. As such, the positions of inter-swathe gaps, in the western and extreme eastern basins at 0600 and in the Ionian Sea at 1800 UTC (Figure 1), change from day to day as well.

The kinetic energy (KE) versus spatial wavenumber (k) power spectra for SVW retrievals from QuikSCAT are distinct from KE power spectra for SVW analyses from ECMWF. The inset in Figure 2 locates the positions of spatial series extracted from ECMWF analyses (red) and across portions of QuikSCAT swathes (black). The ECMWF line and QuikSCAT cross-swathe locations in these spatial series roughly coincide in the southern portions of the western and eastern basins of the Mediterranean Sea, where the longest continuous series can be obtained.

Figure 2 depicts the KE spectra for the zonal wind components from ECMWF and QuikSCAT collected in the spatial series denoted in Figure 2 (map inset). In computing the zonal wind KE spectra, ECMWF spatial series were only used when a corresponding QuikSCAT cross-swathe spatial series was also available. Separate spectra are drawn for each calendar year 2000–2008. This comparison is typical. QuikSCAT KE spectra exhibit an approximate power-law relation (i.e. a constant spectral slope) with KE proportional to wavenumber k^{-2}, down to the Nyquist wavenumber (spatial scales $2\pi/k \sim 50$ km). Conversely, the KE spectra from ECMWF analyses depart from a k^{-2} spectral slope at spatial scales of about 500 km, which is very coarse compared with their output resolution (0.5°). Near the Nyquist wavenumbers, the KE amplitude differences are more than two orders of magnitude for the period 2000–2005. Since January 2002, QuikSCAT winds have been assimilated in the ECMWF analyses but this does not seem to have improved the KE content of the analysis zonal winds. The KE deficit in ECMWF zonal winds ameliorates to just more than 1 order of magnitude in 2006 and thereafter (dash–dotted lines in Figure 2), probably

[†]ECMWF analysis winds are provided on a Gaussian grid transformed from the spectral truncation of the ECMWF forecast model. For the period of 2000–February 2006, the ECMWF operational spectral truncation was $T511$, corresponding to a Gaussian grid resolution of about 40 km. In February 2006, the model resolution was increased to $T799$ or about 25 km. In January 2010 the forecast-model resolution was further enhanced to $T1279$ or about 16 km (see Postscript).

[‡]The QuikSCAT mission ended due to failures in the rotating antenna in late November 2009, just after the original submission of this article. Ocean vector wind retrievals from spaceborne systems are currently available from the ASCAT system on the METOP spacecraft (see Postscript).

[§]In this study we used the R1 version of the QuikSCAT science-quality dataset. At the time of this work, QuikSCAT retrieval algorithms were being updated and an R2 version of the dataset has since been released. See http://podaac.jpl.nasa.gov/DATA_CATALOG/quikscatinfo.html.

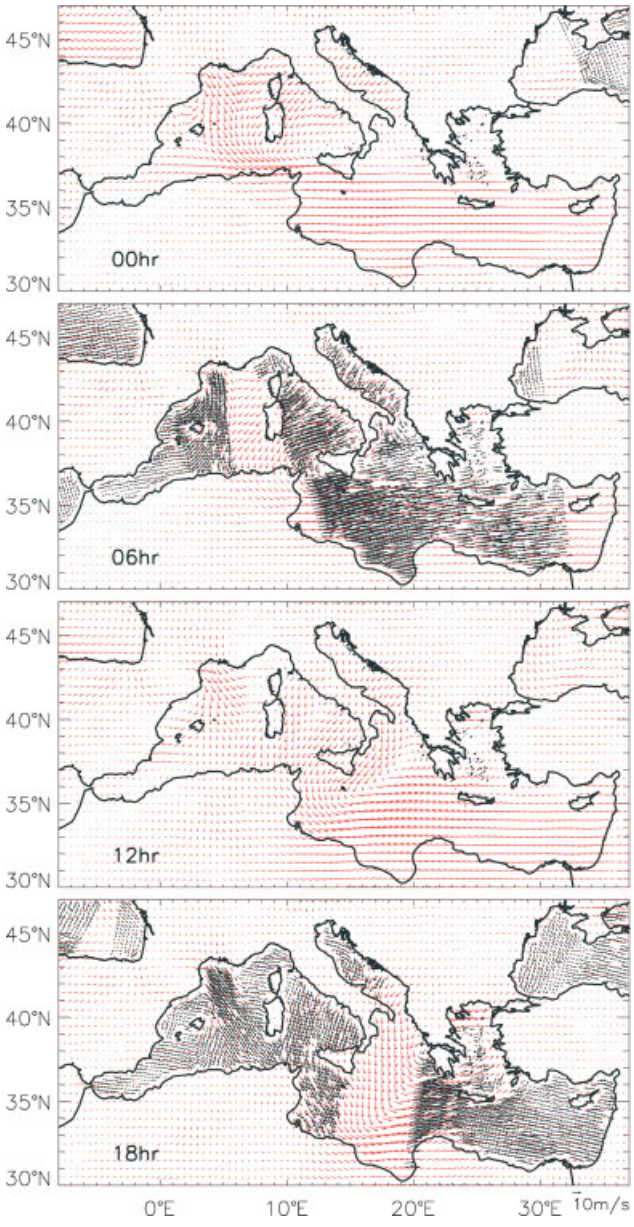

Figure 1. Sample data-stage inputs for the BHM–SVW from 2 February 2005. Data-stage inputs occur at (from top panel to bottom panel) 0000, 0600, 1200 and 1800 UTC every day. Red vectors over the Mediterranean Sea depict the SVW data-stage inputs from the ECMWF analyses and forecasts on a regular 0.5° grid. Black vectors depict higher resolution (25 km) but spatially intermittent SVW retrievals from QuikSCAT. SVW vectors in the QuikSCAT swathe overlay ECMWF analysis vectors nearest in time to the overflight (i.e. ±3 h).

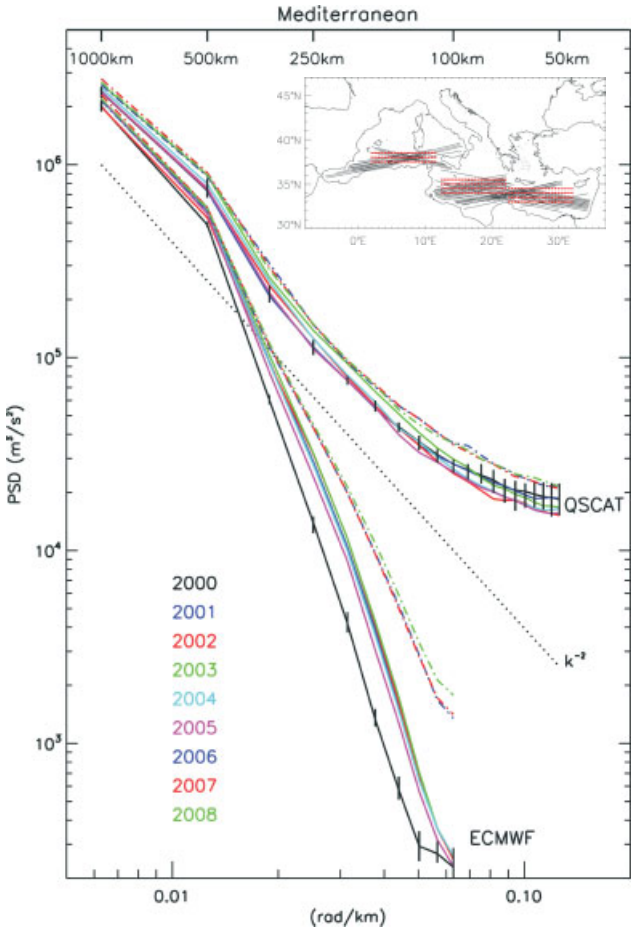

Figure 2. Zonal wind kinetic energy (KE) versus spatial wavenumber (k) for nine years, 2000–2008 (see colors), from ECMWF and QuikSCAT. The longest continuous spatial series for SVW occur in the southern halves of the eastern and western basins of the Mediterranean Sea. Zonal wind spatial series from ECMWF are collected along zonal lines in red (see map inset), and spatial series for QuikSCAT are collected along cross-swathe lines in the same regions (see map inset, black lines). Typical annual spreads in monthly average KE versus k spectral values are noted on the spectra for 2000. The KE content in zonal wind spectra for recent years (2006–2008, dash–dotted lines) has increased in conjunction with ECMWF forecast-model resolution (i.e. model resolution increased from $T511$ for 2000–2005 to $T799$ in 2006). A small increase in the KE content of the QSCAT spectra is probably due to a change in the datasets used (i.e. the R2 data were used for the years 2006–2008 (dash–dotted lines) since R1 was no longer available). Spatial scales (top axis) in km are given by $2\pi/k$.

owing to an increase in ECMWF forecast-model resolution. There is a slight apparent increase in KE amplitudes for the QuikSCAT zonal winds for 2006–2008 as well. Zonal wind retrievals from the older QuikSCAT processing system (R1) were not available after 2005. The small augmentation of KE in 2006 and thereafter is probably due to the change to the R2 dataset.

The KE deficiency of weather-centre analyses at high wavenumbers (spatial scales shorter than several hundred km) is well-known, and has been demonstrated for a very wide variety of locations (Milliff *et al.* 1996, 1999, 2004; Patoux and Brown, 2001; Chelton and Freilich, 2005; Milliff, 2004). Missing power in synoptic and mesoscale winds has important implications for momentum, heat and material property fluxes across the air–sea interface. As noted above, accurate representations of these fluxes and their uncertainties are key to the utility of the SVW field in generating ensemble ocean initial conditions and ensemble ocean forecasts. We will demonstrate in section 3 below that the BHM methodology facilitates the blending of advantages in SVW datasets, including ubiquitous and uniform coverage from ECMWF analyses and realistic high-wavenumber KE content from QuikSCAT SVW. As a result, wind-field realizations from the posterior distribution of a SVW BHM can be used to generate ensemble ocean initial conditions.

2.2. *Scatterometer-based BHM–SVW*

BHMs that produce posterior distributions for the SVW are reported here in a sequence of articles exhibiting increasing volumes in the datasets used and increasing physical sophistication in the design of process models that comprise each successive BHM. Each BHM development involves

problem-specific assumptions driven by, for example, data availability, process-model approximations, feasibility of implementation, etc. Some of these details are noted in the review below. The BHM method adapts well to the operational environment because it can be customized in these ways. A large part of the rest of this article will be devoted to identifying key assumptions and design decisions driven by the application to ensemble initial-condition generation for MFS.

Royle *et al.* (1998) derived a SVW BHM for a single snapshot in time, based on two swathes of scatterometer winds from NSCAT in the Labrador Sea region. The process model in Royle *et al.* (1998) was based on a geostrophic–ageostrophic partition of the SVW field. Sea-level pressure (SLP) was represented by a generic spatial-correlation model with random parameters. The parameters of the geostrophic–ageostrophic model and the spatial-correlation model were estimated in the posterior distribution. The posterior mean SVW and SLP compared well with the ECMWF fields nearest in time for a polar low-pressure system event in the Labrador Sea. A similar geostrophic–ageostrophic process model will be developed in this article.

Wikle *et al.* (2001) create a SVW model for tropical winds based on scatterometer winds from NSCAT and weather-centre winds from NCEP reanalysis. The process-model component of the Wikle *et al.* (2001) BHM is based on the normal modes of the equatorial β-plane (at large scales) and a turbulence closure model based on observed KE spectra for the tropical surface winds (Wikle *et al.*, 1999). The closure-model part is implemented using multiresolution wavelet bases. Realistic surface-convergence features in the posterior mean winds correspond well with intense atmospheric deep convection and rain-band signatures in infrared cloud imagery during the mature phase of the tropical cyclone Dale life-cycle. Hoar *et al.* (2003) extended the Wikle *et al.* (2001) model to generate a multiyear dataset of 50 realizations of the SVW in the tropical Indian and western Pacific Ocean, based on SVW from QuikSCAT retrievals and the NCEP FNL analyses. Multiresolution wavelet bases are used as part of the error process model in the BHM–SVW to be developed here.

Berliner *et al.* (2003) demonstrated BHM capabilities with multiplatform observations in data-stage distributions for an idealized air–sea interaction model in a high-latitude partially enclosed sea. Simulated scatterometer and altimeter data were created for a hypothetical propagating low-pressure system. Spatial and temporal variability in ocean streamfunction uncertainty were derived from the spread of the posterior distribution.

Each BHM development is unique to the setting and practical scale of the particular SVW application. The BHM formalism makes explicit the assumptions regarding the error properties of observations, approximate physics and Bayesian solution procedures. The development of the BHM–SVW is presented in detail here to demonstrate the larger role played by physical reasoning in the design of BHM–SVW relative to past developments based on scatterometer data-stage inputs. Ensemble initial conditions are described here for a single analysis period in MFS as the primary output of the ensemble generation method based on BHM–SVW. In the companion article, the impacts of the BHM–SVW ensemble method on the ocean forecast for this case are examined and statistics for MFS ocean ensemble forecasts are presented and compared with more traditional methods for ensemble forecasting (Part 2).

2.3. *MFS operations*

The MFS is a long-lived operational ocean forecast system that has been producing regular 10 day forecasts every week since January 2000, and every day since September 2004. MFS is comprised of a data-assimilation system and an ocean forecast model. Updates and improvements in both components are always under development. The details of the forecast model will be described in Part 2 (see also Tonani *et al.*, 2008). For now, we note that the model horizontal resolution is $1/16^\circ \times 1/16^\circ$. The vertical dimension is discretized into 72 unevenly spaced vertical levels, resolving the upper ocean at scales of the order of tens of metres. The multivariate data assimilation system at the time of this research was a reduced-order optimal interpolation scheme called the System for Ocean Forecast and Analysis (SOFA: Dobricic *et al.*, 2005, 2007). Input data streams include satellite-derived sea-surface temperature (SST) and sea-level anomaly composites and salinity and temperature profiles from volunteer observing-ship XBT casts and drifting buoys (e.g. Argo).

The data-assimilation procedure in MFS spans 14 days prior to the initial condition time. MFS observations are collected for each day and assimilated to create daily analyses denoted by days 1*A*–14*A*, where day 14*A* at noon is the ocean forecast initial condition. The daily model integrations during the analysis period are forced by surface variable fields from ECMWF analyses in the operational system. The MFS operational model forecast (i.e. days 1*F*–10*F*) is forced by ECMWF forecast winds. We will replace the wind forcing with realizations from the BHM–SVW in this study. Each SVW realization time series spans 24 days: 14 days for the MFS analysis period and 10 days for the MFS forecast period. Over the 14 day analysis period, each SVW realization time series will force a unique ocean initial condition in concert with the aforementioned time-scales for wind-driven adiabatic instability processes in the ocean.

3. BHM design

The BHM design discussion in this section follows a format developed by Berliner *et al.* (2003) that was used to provide background for BHM applications in a variety of geophysical systems. The discussion begins with the introduction of Bayes' theorem, which is general, and is therefore described at a high level of abstraction so as to highlight important modelling components that will be made more specific to the design of BHM–SVW later in the section. For later reference, the doctoral dissertation of Bonazzi (2008) describes BHM design details specific to the MFS application for a version of BHM–SVW that predates the one presented here.

3.1. *BHM design concepts*

Let W be a vector of SVW for all grid locations and every input time in an MFS assimilation cycle and let $[W]$ [¶] be the

[¶] Here and in the following, we often suppress explicit indices for time and space dependence for simplicity. We adopt a common notation such that $[A]$ denotes a probability distribution for a random variable A,

probability distribution of realizations of W. The properties of $[W]$ can be used to quantify the best estimates of the SVW and their uncertainties. The estimates and uncertainties in W are functions of relevant observations D and prior estimates or models for the SVW. Bayes' theorem relates the posterior distribution for the SVW, given data, to three terms in the form

$$[W, \theta_d, \theta_p | D] \propto [D|W, \theta_d][W|\theta_p][\theta_p, \theta_d], \qquad (1)$$

where the left-hand side of (1) is the posterior distribution for W, θ_d and θ_p given the data D. This is the output of interest. The right-hand side of (1) is the product of three distributions that summarize the model hierarchies to be described. The data-stage distribution is $[D|W, \theta_d]$. It is the distribution of the data we expect given the true value of W that we cannot know, but we can measure and model with uncertainties. Measurement error models and/or retrieval algorithms are parametrized in $[\theta_d]$. The process-model stage or 'prior' is $[W|\theta_p]$, where we specify our model for W including parametrizations that can be contained in $[\theta_p]$. Finally, as noted, $[\theta_d]$ and $[\theta_p]$ are probability distributions for estimates of the parameters that arise in the description of the observing system and prior models for W.

Equation (1) is expressed as a proportionality. The quantity $\int [D|W, \theta_d][W|\theta_p][\theta_p, \theta_d]\, \mathrm{d}W\, \mathrm{d}\theta_p\, \mathrm{d}\theta_d$ normalizes the right-hand side of (1) and ensures that the posterior distribution integrates to 1. However, this integral is not tractable in complex settings such as those considered here. The advent of Markov Chain Monte Carlo (MCMC; Robert and Casella, 2004) methods to sample directly from estimates of the posterior has led to the implementations of BHM in very large state-space systems.

The model formulation in (1) is expanded below as we specify details of our application of Bayes' theorem in BHM–SVW. Changes in notation relative to (1) signify specifics within the data-stage distribution and process-model distribution hierarchies. Explicit examples of data-stage and process-model stage parameters will also be identified. In the following, we let $[W] = [U][V]$ for the zonal and meridional components of the SVW. When data-stage and process-model designs are identical for each component, expressions for only one component will be presented. Full expressions for each stage of the BHM–SVW hierarchy are provided in Appendix A. The BHM–SVW output resolutions are 0.5° every 6 h.

3.2. Data-stage distribution design

The data-stage distribution is expanded to incorporate multiple data sources (e.g. SVW from QuikSCAT and ECMWF analyses and forecasts) in the hierarchy for the data-stage distribution component. In BHM–SVW, each component of the SVW is related to spatial gradients of the SLP. This leads to an additional data-stage distribution for SLP 'observations', also from ECMWF analyses and forecasts. Data-stage distributions are adapted from measurement-error models for the scatterometer system, and analysis versus forecast comparisons for SVW and SLP from ECMWF (see Figure 1; see also Chelton and Freilich, 2005). For the QuikSCAT data we let

$$\mathbf{D}^{\mathrm{s}}_{u,t} | \mathbf{U}_t, \mathbf{K}^{\mathrm{s}}_t \sim N(\mathbf{K}^{\mathrm{s}}_t \mathbf{U}_t, \sigma^2_{\mathrm{s}} \mathbf{I}), \qquad (2)$$

which reads, 'The distribution of scatterometer observations of the zonal wind $\mathbf{D}^{\mathrm{s}}_{u,t}$ at time t, given the true zonal winds $\mathbf{U}_t$ and an incidence operator $\mathbf{K}^{\mathrm{s}}_t$ that defines $\mathbf{U}_t$ on the target grid, is prescribed to be a normal distribution[‖] with mean value given by the interpolated true wind and variance given by σ^2_{s}'. The 'true winds' are not known, but from measurement error models (Freilich, 1997; Draper and Long, 2002; Ebuchi *et al.*, 2002; Freilich and Vanhoff, 2003) we characterize the *distribution* of measurements we can expect. Note that $\mathbf{K}^{\mathrm{s}}_t$ and σ^2_{s} are components of θ_d in (1). We choose to specify exact values for these quantities (see Appendix B).

In (2) we have specified a simple Gaussian distribution at each location on the output 0.5° grid about an unbiased mean, with sitewise variances σ^2_{s} taken from the literature. More complicated data-stage models could conceivably include bias terms, sophisticated incidence operators and even model functional formulations to convert radar backscatter data to SVW. We have chosen to use retrieved winds and straightforward models for uncertainty given prior experience with the high-quality data from QuikSCAT.

Data-stage distributions of similar forms are prescribed for the ECMWF SVW and SLP inputs (i.e. for the ECMWF SVW $\mathbf{D}^{\mathrm{e}}_{u,t} | \mathbf{U}_t, \mathbf{K}^{\mathrm{e}} \sim N(\mathbf{K}^{\mathrm{e}} \mathbf{U}_t, \sigma^2_{\mathrm{e}} \mathbf{I})$; note that the mapping matrix $\mathbf{K}^{\mathrm{e}}$ does not vary in time in this case since the ECMWF observation grid does not change during the analysis and forecast periods). Variance terms in the SVW data-stage inputs from ECMWF (i.e. σ^2_{e}) are estimated by comparing basin-wide statistics for QuikSCAT winds with the basin-scale statistics from ECMWF over several annual cycles (values provided in Appendix B). Correlated errors in u and v are not accounted for in the data-stage distribution specifications for QuikSCAT and ECMWF winds. Correlated errors would be modelled in off-diagonal terms of the error covariance matrices (now modelled as diagonal matrices $\sigma^2_{\mathrm{s}} \mathbf{I}$ and $\sigma^2_{\mathrm{e}} \mathbf{I}$). It has been our experience that the incremental addition to model fidelity in specifying off-diagonal terms does not justify the additional costs in model complexity or computations.

The likely increases in uncertainties for surface winds and SLP as functions of forecast lead time versus fixed uncertainties during the analysis period were not accounted for in the data-stage distribution specifications used here. This is discussed in greater detail in Part 2. In future enhancements of the BHM–SVW for the Mediterranean, the variance terms in data-stage distributions of the form (2) can be made time-dependent to accommodate increasing uncertainty during the forecast period.

3.3. Process-model stage distribution design

Building on prior work (Royle *et al.*, 1998), we begin with a geostrophic–ageostrophic partition of the SVW in the process-model design. Expanding on the process-model

$[A, B]$ is the joint distribution for A and B and $[A|B]$ is the conditional distribution of A given the distribution for B.

[‖] $N(\mathbf{a}, \mathbf{b})$ denotes a multivariate normal (or Gaussian) distribution with mean $\mathbf{a}$ and covariance matrix $\mathbf{b}$. $\mathbf{I}$ is the identity matrix, so $\sigma^2_{\mathrm{s}} \mathbf{I}$ is a matrix with the QuikSCAT measurement-error variance on the diagonal. The '[ ]' notation in (1) is not used in assignment expressions such as (2). See also Appendix A.

concepts in earlier BHMs, a Rayleigh friction equation (RFE; Stevens *et al.*, 2002) model is invoked to include surface friction effects explicitly. The RFE model is an approximation of the full momentum and thermodynamic equations for the surface wind (3). This is a model design choice made in light of the volume and precision of the QuikSCAT inputs to the data-stage distribution. There are no comparable coincident satellite observations of boundary-layer and air–sea interface thermodynamic terms (i.e. temperature and moisture gradients) to augment the high-resolution, high-precision SVW data from QuikSCAT. Therefore, we did not introduce explicit thermodynamic terms and coefficients in the process model. Nonetheless, the SVWs from QuikSCAT data contain the thermodynamic effects that lead to the vector wind signal measured by the satellite. In deciding to base the process-model stage on approximations of the RFE, we have not neglected thermodynamic effects, but rather relied upon data that includes the effects of thermodynamic processes. Bayes' theorem (1) yields posterior distributions that are weighted combinations of the data and process models. The data enter (1) via the data-stage distribution. Similar arguments pertain to the implicit treatment of neglected (e.g. non-linear) terms in the momentum equations as well.

The RFE are given by

$$\begin{aligned} \frac{\partial u}{\partial t} - fv &= -\frac{1}{\rho_o}\frac{\partial p}{\partial x} - \gamma u, \\ \frac{\partial v}{\partial t} + fu &= -\frac{1}{\rho_o}\frac{\partial p}{\partial y} - \gamma v, \end{aligned} \tag{3}$$

where f is the Coriolis term, ρ_o is the reference atmospheric density, p is SLP and γ is the Rayleigh friction term. The SLP anomaly is decomposed into a summation of m spatial structure functions $\phi_k(x, y)$, $k = 1, \ldots, m$, each multiplied by time-dependent scalar weights $a_k(t)$:

$$p(x, y, t) = \mu + \sum_{k=1}^{m} a_k(t)\, \phi_k(x, y). \tag{4}$$

We have computed $m = 20$ spatial eigenvectors for the ϕ_k in (4), after removing a mean SLP (μ) from a seasonal time series of ECMWF SLP analyses for the Mediterranean region. On average, 20 ϕ_k were sufficient to project 80% of the variability in the SLP anomaly fields over the seasonal time series.

The momentum equations (3) can be rearranged into (1) an equation in zonal velocity u that depends only on u (and not v) and SLP time-derivative and spatial-gradient terms and (2) an equation in v not depending on u and similar SLP spatial-gradient and time-derivative terms. These are given by

$$\begin{aligned} \frac{1}{f}\left[\frac{\partial^2}{\partial t^2} + (f^2 + \gamma^2)\right] u + 2\frac{\gamma}{f}\frac{\partial u}{\partial t} \\ = -\frac{1}{\rho_o}\frac{\partial p}{\partial y} - \frac{1}{\rho_o f}\frac{\partial^2 p}{\partial x \partial t} - \frac{\gamma}{\rho_o f}\frac{\partial p}{\partial x}, \end{aligned} \tag{5}$$

$$\begin{aligned} \frac{1}{f}\left[\frac{\partial^2}{\partial t^2} + (f^2 + \gamma^2)\right] v + 2\frac{\gamma}{f}\frac{\partial v}{\partial t} \\ = \frac{1}{\rho_o}\frac{\partial p}{\partial x} - \frac{1}{\rho_o f}\frac{\partial^2 p}{\partial y \partial t} - \frac{\gamma}{\rho_o f}\frac{\partial p}{\partial y}. \end{aligned}$$

In the process model to be developed here, we eliminate explicit time-derivative terms from (5), yielding a geostrophic–ageostrophic model similar to the process model in Royle *et al.* (1998). The model design choice to include explicit terms only for geostrophic and ageostrophic pressure gradients is essentially *ad hoc*. A more systematic approach to process-model design is a subject of current research. Nonetheless, the geostrophic–ageostrophic truncation of the RFE can be written as

$$\left.\begin{aligned} u &= -\frac{f}{\rho_o(f^2 + \gamma^2)}\frac{\partial p}{\partial y} - \frac{\gamma}{\rho_o(f^2 + \gamma^2)}\frac{\partial p}{\partial x}, \\ v &= \frac{f}{\rho_o(f^2 + \gamma^2)}\frac{\partial p}{\partial x} - \frac{\gamma}{\rho_o(f^2 + \gamma^2)}\frac{\partial p}{\partial y}. \end{aligned}\right\} \tag{6}$$

These are the expressions, in continuous form, that lead to the process-model component of the BHM–SVW. Bonazzi (2008) explores a second atmospheric model form wherein more terms from the RFE are made explicit.

The velocity fields implied by (6) are unravelled into column vectors of velocity components and discrete forms for (6) are obtained by centred-space approximations. In matrix notation we have

$$\left.\begin{aligned} \mathbf{U}_t &= -\frac{f}{\rho_o(f^2 + \gamma^2)}\mathbf{D}_y\mathbf{P}_t - \frac{\gamma}{\rho_o(f^2 + \gamma^2)}\mathbf{D}_x\mathbf{P}_t, \\ \mathbf{V}_t &= \frac{f}{\rho_o(f^2 + \gamma^2)}\mathbf{D}_x\mathbf{P}_t - \frac{\gamma}{\rho_o(f^2 + \gamma^2)}\mathbf{D}_y\mathbf{P}_t, \end{aligned}\right\} \tag{7}$$

where the discrete estimate for vectorized u at time t is $\mathbf{U}_t$, the SLP at time t is $\mathbf{P}_t$ and $\mathbf{D}_{x,y}$ are the discrete operators for the spatial derivatives. The important conceptual leap to a stochastic form for (7) is given by a relatively subtle notational change in the equations as

$$\left.\begin{aligned} \mathbf{U}_t &= a_{1,1}\mathbf{D}_y\mathbf{P}_t + a_{1,2}\mathbf{D}_x\mathbf{P}_t + \boldsymbol{\epsilon}_{u,t}, \\ \mathbf{V}_t &= b_{1,1}\mathbf{D}_x\mathbf{P}_t + b_{1,2}\mathbf{D}_y\mathbf{P}_t + \boldsymbol{\epsilon}_{v,t}, \end{aligned}\right\} \tag{8}$$

where $\boldsymbol{\epsilon}_{u,t}$ and $\boldsymbol{\epsilon}_{v,t}$ are random error vectors to be described. A stochastic form for the SLP decomposition (4) is

$$P_t(x, y) = \mu + \sum_{k=1}^{N} \alpha_{k,t}\, \phi_k(x, y). \tag{9}$$

Here, the coefficients $a_{1,1}$, $a_{1,2}$, $b_{1,1}$, $b_{1,2}$ and $\alpha_{k,t}$ in (8) and (9) are assumed to be random and therefore endowed with probability distributions to be prescribed at the next level of the hierarchy. In other words, $a_{1,j}$, $b_{1,j}$ and $\alpha_{k,t}$ are some of the parameters contained in θ_p (see (1)) for the BHM–SVW. The $a_{1,j}$, $b_{1,j}$ for $j = 1, 2$ are independent of time and location in the current formulation of BHM–SVW. Adding space and time dependence increases the computational burden of the model beyond that desired for this first implementation in an operational ocean forecast system setting. The $\alpha_{k,t}$ are allowed to vary with each discrete time step, but no explicit time-dependence model is imposed because the SLP data are complete and project on to these coefficients such that the reconstructed SLP evolution is realistically smooth.

Prior distributions for the random coefficients $a_{1,j}$, $b_{1,j}$ and $\alpha_{k,t}$ are

$$\left.\begin{aligned} a_{1,1} &\sim N\left(-\frac{f}{\rho_o(f^2+\gamma^2)}, \sigma^2_{a_{11}}\right), \\ a_{1,2} &\sim N\left(-\frac{\gamma}{\rho_o(f^2+\gamma^2)}, \sigma^2_{a_{12}}\right), \\ b_{1,1} &\sim N\left(\frac{f}{\rho_o(f^2+\gamma^2)}, \sigma^2_{b_{11}}\right), \\ b_{1,2} &\sim N\left(-\frac{\gamma}{\rho_o(f^2+\gamma^2)}, \sigma^2_{b_{12}}\right), \\ \alpha_{k,t} &\sim N(0, \sigma^2_P). \end{aligned}\right\} \quad (10)$$

Values used for the parameters of these distributions ($\sigma^2_{a_{11}}$ etc.) are listed in Appendix B.

The $\boldsymbol{\epsilon}_{u,t}$ and $\boldsymbol{\epsilon}_{v,t}$ terms represent the process-model uncertainty in (8). They are defined at the next level of the process-model hierarchy in (11) below. More generally, these terms can be thought of as 'model misfit' terms that measure the representativeness of the process model. In this sense, $\boldsymbol{\epsilon}_{u,t}$ and $\boldsymbol{\epsilon}_{v,t}$ include the combined effects of unknown distributions corresponding to terms excluded in the truncation of the RFE, as well as the unknown impacts of terms and physical processes that are not part of the RFE (e.g. thermodynamic processes). Recall from (1) that the $\boldsymbol{\epsilon}_{u,t}$ and $\boldsymbol{\epsilon}_{v,t}$ are part of the posterior distribution (i.e. under the θ_p hierarchy). If, given the QuikSCAT and ECMWF data, the RFE are not an appropriate starting place for the development of BHM–SVW, or the truncation to a geostrophic–ageostrophic model is too severe, then we expect the amplitudes of the most likely values in the posterior distributions for $\boldsymbol{\epsilon}_{u,t}$ and $\boldsymbol{\epsilon}_{v,t}$ to be greater than the modes of the posterior distributions of the $a_{1,j}$, $b_{1,j}$ in (8) via (10).

The distribution specification for the $\boldsymbol{\epsilon}_{u,t}$ is given by (Bonazzi, 2008)

$$\left.\begin{aligned} \boldsymbol{\epsilon}_{u,t} &= \sum_{k=1}^{n_\beta} \boldsymbol{W}_k \boldsymbol{\beta}^u_{k,t} + \tilde{\boldsymbol{\epsilon}}_{u,t}, \\ \tilde{\boldsymbol{\epsilon}}_{u,t} &\sim N(\mathbf{0}, \sigma^2_u \mathbf{I}). \end{aligned}\right\} \quad (11)$$

The error model is comprised of two parts: (1) a spatially structured part consisting of nested wavelet bases $\boldsymbol{W}_k$, weighted by random coefficients (i.e. $\boldsymbol{\beta}^u_{k,t}$), and (2) a Gaussian noise part (i.e. $\tilde{\boldsymbol{\epsilon}}_{u,t}$), where each $\boldsymbol{\beta}^u_{k,t}$ is assumed to follow an independent auto-regressive process (see Appendix A). An analogous formulation to (11) is given for $\boldsymbol{\epsilon}_{v,t}$. The wavelet bases are adapted from the SVW BHM for tropical winds in Wikle *et al.* (2001). They are imposed, as a complete set, fitted to the finite domain to account for multiscale correlated error processes that were shown to be important, given scatterometer data, by Wikle *et al.* (2001). The BHM methodology allows this more efficient form to replace an explicit model for the full error covariance structure that would not be tractable in a problem with a state-space dimension comparable to ours. While the error-model forms (11) are identical for each velocity component, the errors for $\mathbf{U}_t$ and $\mathbf{V}_t$ are independent, as are the parameters σ^2_u, σ^2_v, $\boldsymbol{\beta}^u_{k,t}$ and $\boldsymbol{\beta}^v_{k,t}$. Conditional distributions for the terms $\boldsymbol{\beta}^u_{k,t}$, $\boldsymbol{\beta}^v_{k,t}$, $k = 1, \ldots, n_\beta$, and σ^2_u, σ^2_v are specified in Appendix A.

3.4. *BHM computation*

Summaries of the variable and parameter posterior distributions are obtained by Markov chain Monte Carlo (MCMC) methods; specifically the Gibbs Sampler (Gilks *et al.*, 1996). The key to the method is to construct a Markov chain on the state and parameter spaces having a limiting distribution coinciding with the target posterior distribution. Then simulated trajectories of this chain, after a relaxation or burn-in period, are approximately realizations for the posterior distribution.

For the Gibbs Sampler, the Markov chain is comprised of a sequence of *full conditional distributions* (Gilks *et al.*, 1996). These full conditional distributions are sampled for the process variables $\mathbf{U}_t$, $\mathbf{V}_t$ and $\mathbf{P}_t$ and the unknown parameters in a sequential fashion. The full conditional distributions used here are described in Appendix A. Results from Markov chain theory imply that the Gibbs Sampler is guaranteed to equilibrate to an ergodic state such that continued samples from the Markov Chain are samples from the posterior distribution (i.e. the left-hand side of (1)). The Gibbs Sampler for the BHM–SVW was coded in MATLAB.** Estimates of the posterior distribution are obtained from the final 80 000 of 100 000 iteration runs of the Gibbs Sampler. A running mean of the posterior distribution was computed after the 20 000 iteration burn-in period to observe convergence of the Markov Chain. Realizations from the posterior distributions were saved at arbitrary intervals in the Gibbs Sampler iterations (i.e. every 8000 iterations). This level of computational effort is not unusual for a hierarchical model with as many state variables, parameters and data-stage inputs as in BHM–SVW.

BHM–SVW was partially validated in a synthetic data experiment wherein a circularly symmetric idealized low-pressure system was propagated along a line of latitude through the Mediterranean Sea domain over 10 days. Synthetic SVWs were computed to be in geostrophic balance with the idealized SLP (i.e. Rayleigh friction $\gamma = 0$). The synthetic winds were sampled with simulated measurement errors according to a data-stage distribution as in (2). Posterior distributions for the parameters (10) were examined after 10 000 iterations of the Gibbs Sampler. The model was validated in that (1) the modes of the Gaussian distributions for $a_{1,1}$ and $b_{1,1}$ in (10) were centred on $\pm 1/f$, i.e. the inverse Coriolis term (which is all that is left in $a_{1,1}$ and $b_{1,1}$ when $\gamma = 0$), and (2) the modes of the distributions for the coefficients $a_{1,2}$ and $b_{1,2}$ were 0, also as required when $\gamma = 0$ (see (10)).

4. BHM–SVW results

BHM–SVW output results are reported in this section. Implications of BHM–SVW for the MFS initial conditions are discussed in the next section and implications for the MFS forecast performance are the topic of Part 2.

Recall that the process-model stage consists of the hierarchy of distributions implied by (8), (9), (10) and (11). The data-stage distributions are based on the SVW from QuikSCAT and the SVW and SLP from ECMWF analyses during the analysis period (days $1A - 14A$), and during the

**MATLAB is a registered trademark of The MathWorks, Inc., 3 Apple Hill Drive, Natick, MA 01760 (508)647-7000 (see http://www.mathworks.com/trademarks).

forecast step (days $1F - 10F$) they are based on SVW and SLP forecasts from ECMWF. In the following we compare the effects of removing the QuikSCAT data from the data-stage inputs with the full data-stage case. Results are described in terms of (1) 'posterior mean' fields and values, i.e. the means of posterior distributions for dependent variables and parameters, and (2) the uncertainty or 'spread' in posterior distributions as quantified by the standard deviation with respect to the posterior mean for a randomly selected set of realizations (usually 10) from the posterior distributions.

Figure 3 is a snapshot from the posterior distribution of the BHM–SVW output in the western basin of the Mediterranean Sea at 1800 UTC on 2 February 2005 (i.e. day 9*A*). Clusters of ten SVWs (black vectors), from 10 realizations of the posterior distribution, emanate from the BHM output grid locations. A red vector denotes the posterior mean SVW at each grid location for this date and time.[††] In regions where the surface winds are strong, the SVW clusters are more uniform in amplitude and direction (note the winds in the Ionian Sea east of Sicily, and in the Mistral region centred on 5°E between 38°N and 42°N). Conversely, in places where the winds are weak, the vector wind direction and amplitude are more uncertain. This is evident in the wider ranges of wind direction among relatively low-amplitude realizations (note the light winds centred on 1°E, between 36.5°N and 41°N). The SVW clusters amplify and contract and spread and collapse, time step by time step, as data-stage and process-model distributions interact (see (A1) in Appendix A) over the analysis and forecast periods.

The blue distributions in Figure 4 depict the posterior distributions for the coefficients in the BHM–SVW process model (i.e. $a_{1,j}$, $b_{1,j}$ for $j = 1, 2$) given the full data-stage distribution. The starting value for each coefficient is noted at the top of each panel. The initial values are determined by evaluating the expressions for the means in (10) for given f, γ and ρ_o. For all coefficients, the modes of the posterior distributions are far from the respective initial values. Nonetheless, the model misfit terms (11) are small (i.e. $\boldsymbol{\epsilon}_{u,t}, \boldsymbol{\epsilon}_{v,t} \leq \mathcal{O}(1\,\mathrm{m\,s^{-1}})$; not shown) throughout the latter 80 000 iterations of the Gibbs Sampler for BHM–SVW. Dynamical interpretations of the posterior distributions of the model parameters are discussed in the next section.

The red distributions in Figure 4 are for the same coefficients and BHM–SVW process-model version, in an experiment where the QuikSCAT data have been excluded from the data-stage distribution during the analysis period. In the absence of QuikSCAT data-stage inputs, the modes of the posterior distributions for the coefficients $a_{1,j}$, $b_{1,j}$ are closer to their initial values and exhibit less spread about their respective modes (Figure 4). The modal values for the $a_{1,j}$, $b_{1,j}$ will be discussed and contrasted for the 'with' and 'without' QuikSCAT data cases in the next section.

It is worth emphasizing here that the QuikSCAT data increase the uncertainty in the parameter distributions for this model, while the model error terms $\boldsymbol{\epsilon}_{u,t}$ and $\boldsymbol{\epsilon}_{v,t}$ from (11) remain small. The final 80 000 iterations of the Gibbs Sampler are depicted for the BHM–SVW process-model parameters in Figure 5. These iteration traces suggest that the model might be approaching an equilibrium state (note the different resolutions on the y-axes in Fig 5). Integrations over the iterations shown in Figure 5 yield the distributions shown in Figure 4.

Figure 6 compares zonal wind KE spectra computed from the BHM–SVW posterior distribution for the analysis period (i.e. days $1A - 14A$). The left-hand panel compares spectra when QuikSCAT data are included in the data-stage distributions for the BHM, and the right-hand panel compares spectra when QuikSCAT data are excluded. In each panel, the spectra include averages over the analysis period from QuikSCAT (green), ECMWF (green dashed), the BHM–SVW posterior mean u (red) and the average spectra from 10 realizations of the posterior distribution for u (black). A line corresponding to a k^{-2} power law is drawn for reference (thin black). The spatial series for these spectra are taken from the tracks identified on the inset to Figure 2. More than 6000 spectra are averaged to produce the realization spectrum (black line), and more than 600 spectra are averaged to produce the posterior mean spectrum (red line).

The BHM–SVW that includes QuikSCAT data-stage distributions (Figure 6, left panel) yields spectral slopes for realizations and for the posterior mean that roughly follow the spectrum computed from QuikSCAT data alone (green solid line), i.e. something like a k^{-2} power-law relation. Closer adherence to the QuikSCAT spectrum might be achieved by tuning uncertainty terms in the distributions assigned to terms and parameters in BHM–SVW (see Appendix A). The average spectrum from ECMWF (green dashed line) demonstrates again the KE deficiency we saw in Figure 2.

The zonal wind KE spectra change dramatically when QuikSCAT data are excluded from the data stage (Figure 6, right panel). In particular note that (1) the average realization spectrum (black line) is flat, departing from the QuikSCAT spectrum (green line) and the k^{-2} line to exhibit uniform and higher KE at higher wavenumbers and (2) the average spectrum for the posterior mean zonal wind (red line) tracks the ECMWF average spectrum (green dashed line). This suggests that the SVW process in the BHM realizations when QuikSCAT data are excluded is dominated by white-noise behaviour at the wavenumbers corresponding to synoptic and mesoscale variability (i.e. from scales $\sim$ 300 km and finer). The noise process in each realization drives zonal wind KE amplitudes in excess of the approximate power-law relation detectable by QuikSCAT. Averaging over all realizations in the posterior distribution (i.e. to obtain the posterior mean) cancels the noise process and the posterior mean spectrum (red) reflects the zonal wind KE deficiency already noted in the ECMWF SVW (i.e. Figure 2). The noise process in each realization can arise from the combined effects of the uncertainty terms that are made explicit for data-stage and process-model stage terms at the extremes of the model hierarchies (e.g. the variance terms in Appendices A and B).

5. Discussion

The BHM–SVW development experiments have quantified, in probabilistic terms, aspects of the dynamics and uncertainty of the SVW over the Mediterranean Sea. This begins to demonstrate the quantitative value of BHM in large state-space applications. In the first part of the discussion

[††]Recall that the posterior mean SVW is the average over the posterior distribution, consisting of 80 000 realizations after the burn-in. The black vectors are single realizations taken every 8000 iterations of the Gibbs Sampler.

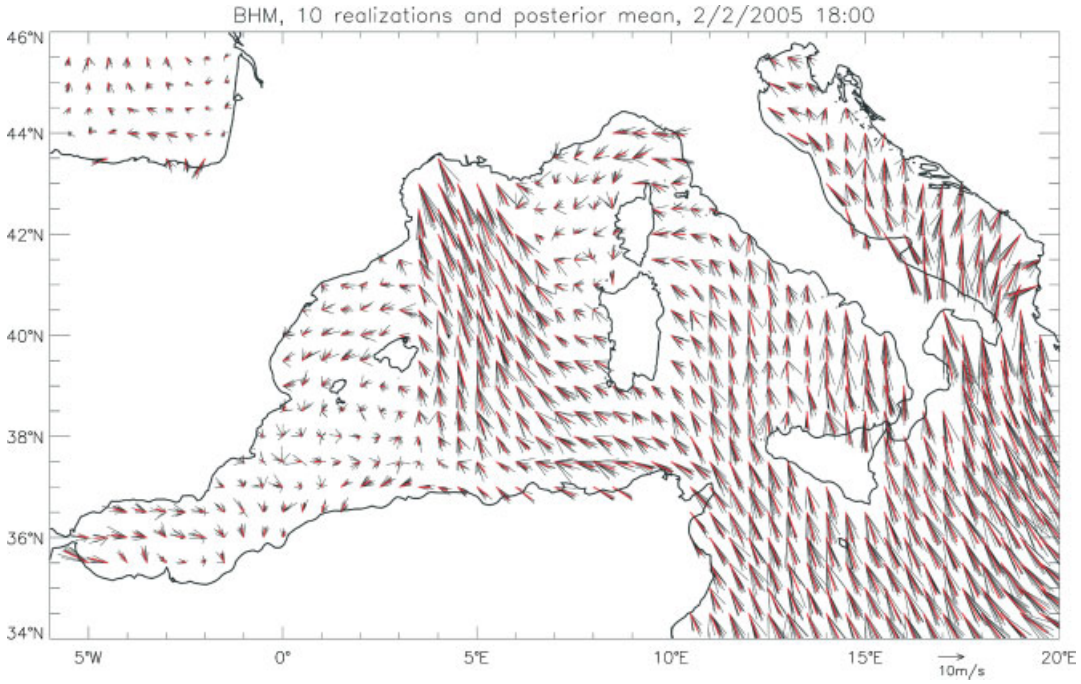

Figure 3. Sample SVW realizations from the posterior distribution of BHM–SVW for the western Mediterranean basin on 2 February 2005 at 1800 UTC. Ten wind vectors (black) are plotted at each BHM output grid location for this snapshot. A red vector at each location represents the posterior mean surface wind vector at each location for this time. The wind magnitude (line length) and direction for each of the realizations are represented by black lines emanating from each BHM grid location. The snapshot corresponds to day 9*A* during the data-assimilation period for the reforecast experiment. The Mistral winds are freshening in the Gulf of Lyon, and strong north–northwest winds are evident in the region of the Sicily Straits. Where wind speeds are large (i.e. in the region of the Mistral), the ensemble winds are more narrowly distributed about the posterior mean wind. In sheltered regions (i.e. southwest of Minorca, e.g. 1°E, 38°N), the wind speeds are low and direction uncertainty is larger.

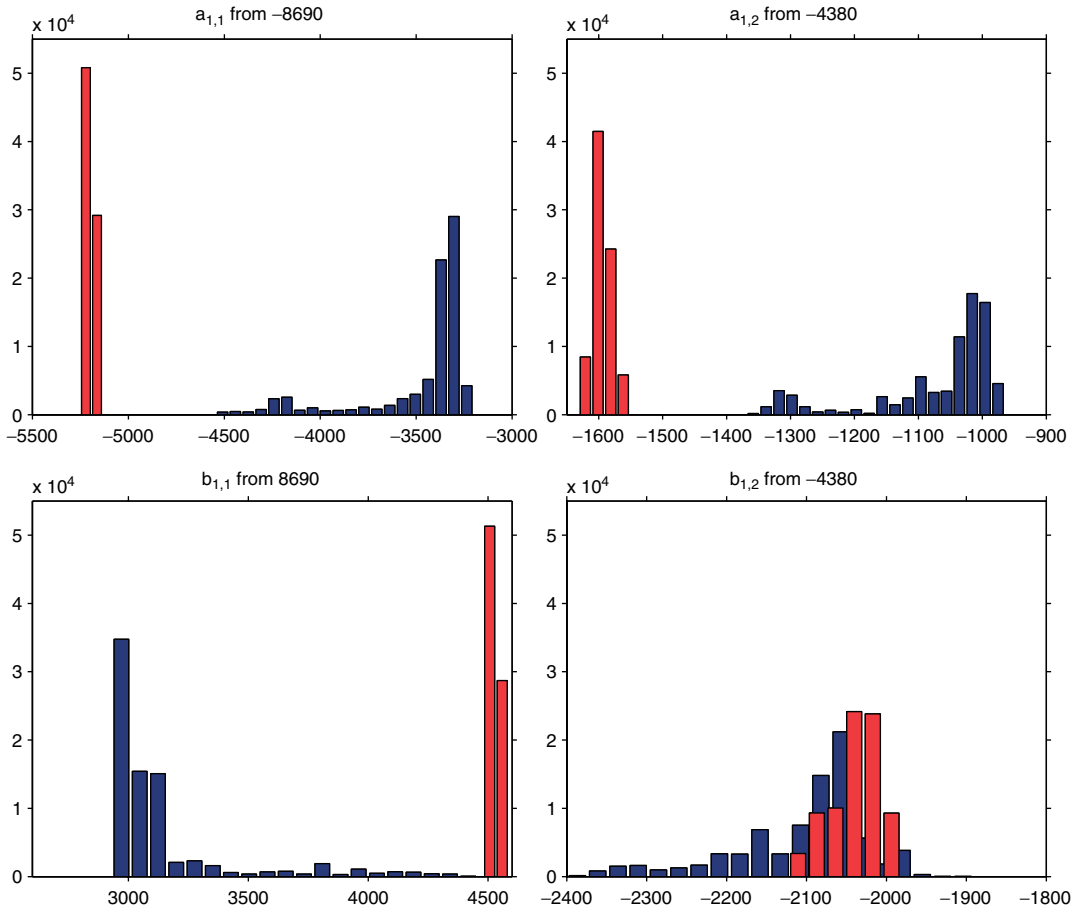

Figure 4. Posterior distributions for the process-model coefficients $a_{1,j}$, $b_{1,j}$ for $j = 1, 2$ of the BHM–SVW. Posterior distributions are accumulated from the last 80 000 iterations of a 100 000 iteration Gibbs Sampler implementation. Blue distributions are for a BHM–SVW implementation that includes QuikSCAT data-stage inputs and red distributions are from an implementation that excludes QuikSCAT data. Coefficient initial values (i.e. at iteration 0) are noted in each panel.

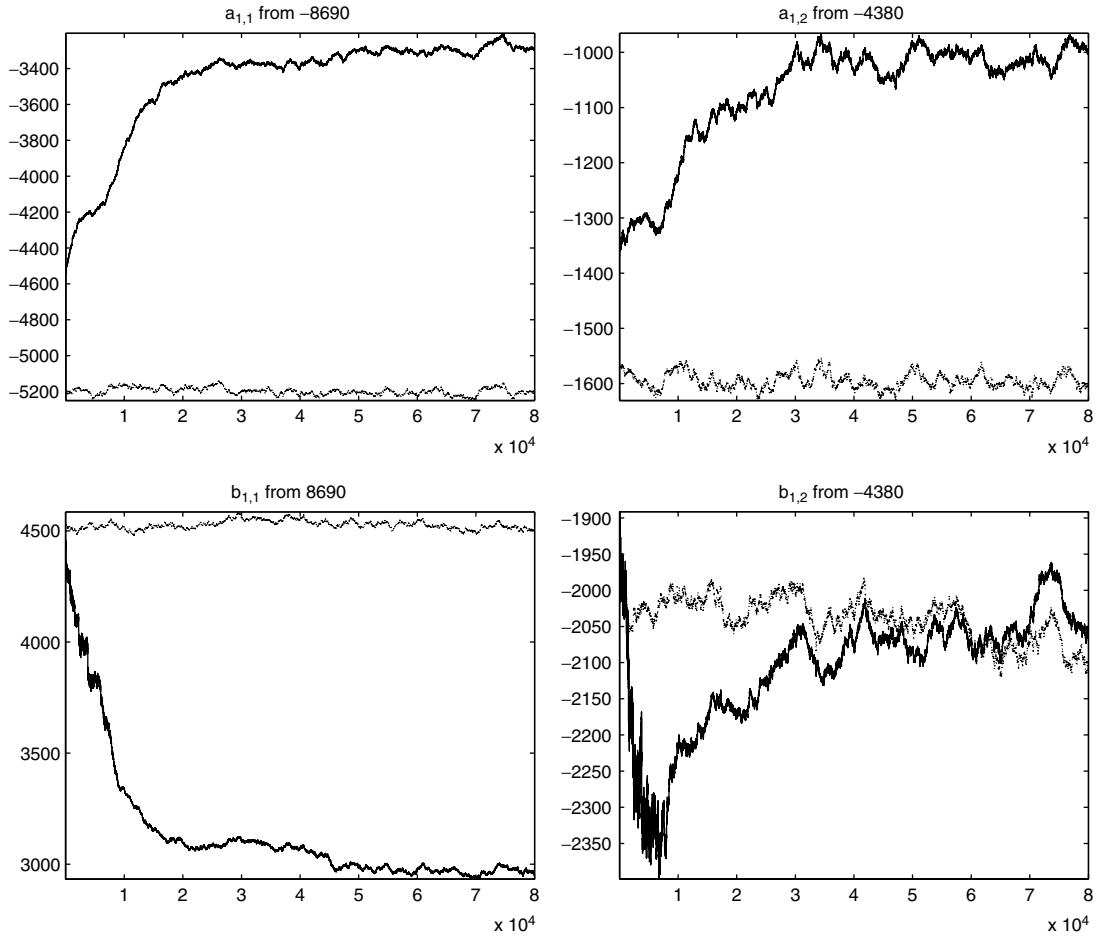

Figure 5. Iteration traces for process-model parameters from the final 80 000 iterations of the Gibbs Sampler for the BHM–SVW. The solid line traces the BHM iterations when QuikSCAT data-stage inputs are included. The dotted line marks the QuikSCAT-excluded iteration traces. Parameter values are on the *y*-axes and Gibbs Sampler iteration numbers are on the *x*-axes. Parameter initial values are noted in each panel. The distributions in Figure 4 are the summations over all iterations of the traces shown here.

section we explore issues of quantitative validation arising from our experiments with BHM–SVW thus far. The validation exercises we propose are the foci of ongoing research.

The chief purpose of the BHM–SVW development is to provide a method, based on multiplatform data and appropriate physical reasoning, for the generation of physically realistic ensemble surface-wind forcings leading to ocean ensemble initial conditions. The BHM–SVW method is a new means of achieving this goal, and it is evaluated in comparisons with more traditional ocean initial-condition generation and ocean ensemble forecast methods for MFS in a companion article (Part 2). In the second part of the discussion section here, we describe ensemble initial condition impacts for the single analysis test case we have been studying so far.

5.1. *Probabilistic quantification of the SVW dynamics*

The physical interpretation associated with the truncated RFE that led to the BHM–SVW process model supposes that the SVW components can be represented by geostrophic (i.e. across the SLP gradient) and ageostrophic (i.e. along the SLP gradient) diagnostic terms. Moreover, the geostrophic–ageostrophic interpretation is posed for the particular spatial and temporal resolution of the BHM–SVW (i.e. 0.5° and 6 h). If the geostrophic–ageostrophic model is sufficient to capture the dynamics of the SVW for most of the grid locations in the Mediterranean domain, for most of the time steps in the analysis and forecast periods, then the initial parameter distributions would change very little in the presence of the data-stage distributions.

This turned out not to be the case (see Figure 4). Instead, the data-stage and process-model stage distribution interactions led to posterior distributions for the BHM–SVW parameters that are (1) centred on values very different from initial values and (2) sensitive to the presence of QuikSCAT inputs in the data-stage distribution. It is important to note that the misfit terms ($\boldsymbol{\epsilon}_{u,t}$ and $\boldsymbol{\epsilon}_{v,t}$) remained small throughout the Gibbs iterations to generate the posterior distribution.

The change in modes from initial values to the posterior means for the distributions for parameters $a_{1,j}$, $b_{1,j}$ is an example of 'Bayesian learning'. In the posterior, influence from the data-stage distribution terms mixes with the process-model terms. There is no guarantee that the initial physical interpretations of pressure-gradient terms will be retained as Bayesian learning occurs. However, we know that the posterior distributions of these parameters do have physical interpretations in the limiting case of purely geostrophic flow in an idealized cyclone (not shown). Moreover, we know that the distributions for model misfit parameters are centred on small amplitudes, so the partition

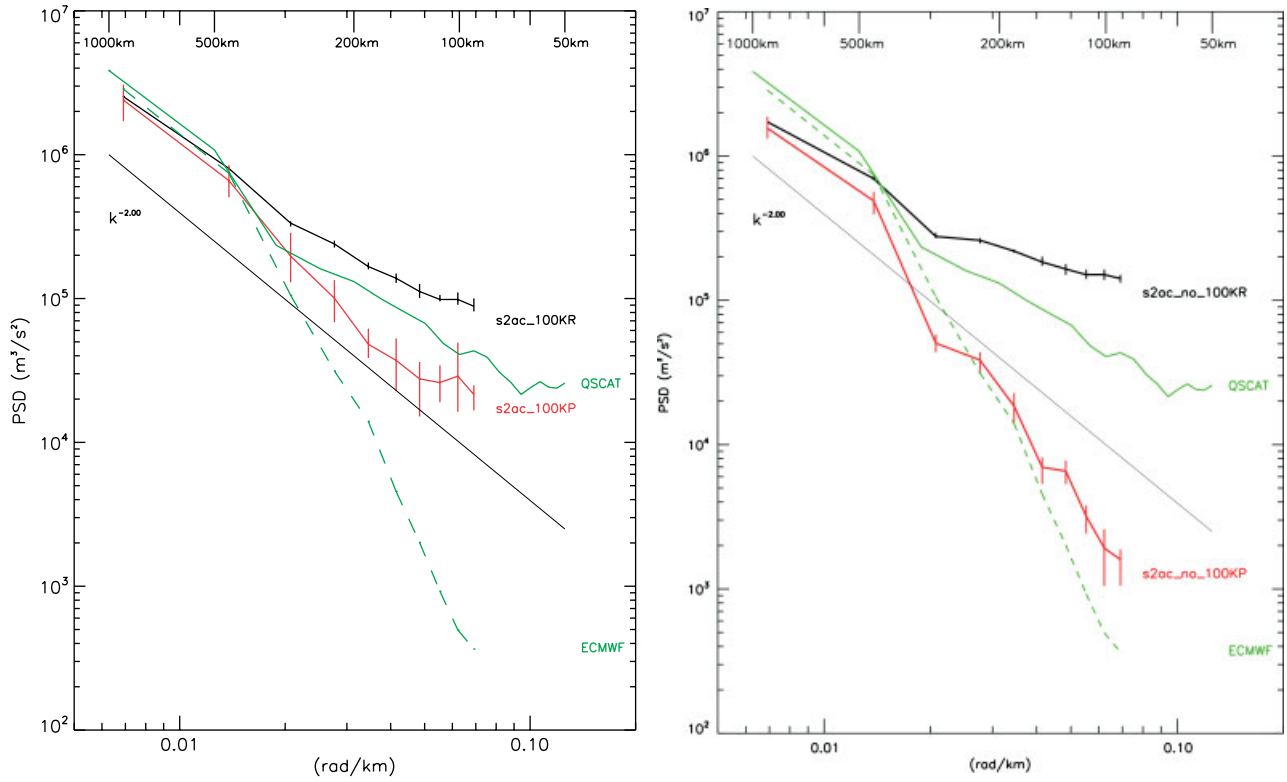

Figure 6. Zonal wind kinetic energy spectra for the analysis period (days 1*A* − 14*A*) for BHM–SVW posterior distributions in experiments that included QuikSCAT winds in the data stage (left panel) and experiments that excluded QuikSCAT (right panel). Each panel exhibits spectra for the posterior mean zonal wind (bold red lines), and for the averages over 10 realizations from the posterior distribution (bold black lines). These are compared with average spectra for the same period from QuikSCAT data (green solid lines) and ECMWF analysis winds (green dashed lines). A reference line for a k^{-2} power law is also shown (thin black line). Spatial series are taken from the tracks identified on the inset to Figure 2. Vertical bars at selected wavenumbers indicate the spreads for spectra computed from realizations of the posterior distribution (black) and the posterior mean (red).

of the flow field into along- and across-pressure-gradient terms is reasonably complete in this sense.

The increase in parameter uncertainty (i.e. spread in posterior distributions) when QuikSCAT data are included in the data stage indicates a lack of agreement between the data and the model as it was initially interpreted. For this model and these data, the model misfit terms are not substantially larger when QuikSCAT data are included, but the parameter spreads increase. While the QuikSCAT data add uncertainty to the interpretation of the model parameters, they also improve the posterior mean estimates of the SVW, which is the practical goal of BHM–SVW.

The KE spectra in Figure 6 and the posterior distribution comparisons of the BHM–SVW with and without QuikSCAT data-stage inputs (Figure 4) suggest physical arguments to help interpret the departure from a simple geostrophic–ageostrophic dynamical interpretation for the SVW process over the Mediterranean Sea for the single period 1*A*–10*F* studied here. The analysis and forecast periods span a time-scale that is long enough to contain the developments and propagations of several atmospheric disturbances. Animations (not shown) of the SLP and SVW posterior mean fields clearly demonstrate the developments of several low-pressure systems in the western basin, their subsequent evolution, associated frontal systems and propagation into the eastern Mediterranean over the 24 day period. Dynamical processes associated with these developments are not completely described by the geostrophic–ageostrophic diagnostics in the BHM–SVW process model, but they project on these terms so as to adjust the distributions of the $a_{1,j}$, $b_{1,j}$ for $j = 1, 2$ such that posterior mean values are far from initial values. While these coefficient adjustments are large, the model misfit terms $\epsilon_{u,v}$ remain small and this leads to model validation experiment proposals described below.

The zonal wind KE deficiencies of the ECMWF SVW data inputs (Figure 2) occur on scales commensurate with phenomena associated with low-pressure system development and evolution that is more complicated than the geostrophic–ageostrophic interpretation. No such KE deficiency is evident in the spectra from QuikSCAT data, or from the BHM–SVW that includes QuikSCAT data.

The impacts of terms important for cyclone development and frontal dynamics are represented in the data-stage distributions including QuikSCAT data. They project on to the distributions from diagnostic pressure-gradient terms in the geostrophic–ageostrophic process-model stage and are evident in the realizations and mean fields of the posterior distribution. The impacts of these terms on the posterior distributions for the process-model parameters (Figure 4) is to move the posterior mean away from geostrophic–ageostrophic initial values and to increase the spread about the modes. Research in progress deals with the question of how to validate further the posterior mean values of model parameter distributions given approximations in process-model development, and the complexity of the real system that enters the BHM in the data stage. The spectral analyses presented here (Figure 6) serve as one metric in the validation effort.

In discussing the physical interpretability of the process-model parameters, two means for immediate improvements in BHM–SVW have become apparent. These include (1)

making additional terms in the process models explicit, so as to go beyond the geostrophic–ageostrophic model, which is not providing physically consistent interpretations for the time period and domain of interest, and (2) making process-model parameters time- and/or space-dependent such that regional differences in the wind field will lead to regional differences in parameter posterior distributions. These are objectives of the research in progress. However, as we describe in the next subsection, even this first implementation of BHM–SVW in the MFS provides for physically reasonable and practically useful ensemble initial-condition spread.

5.2. *Ensemble initial conditions and ensemble forecast winds*

The SVW clusters in Figure 3 depict a snapshot of the ensemble of surface winds used to drive ocean analyses and forecasts in MFS. Upper-ocean response differences are implied in the spread of the realizations in the clusters at each location. Ocean dynamics and thermodynamics respond in different proportions to the vector winds (e.g. air–sea heat fluxes), vector wind stresses (e.g. momentum fluxes), wind-stress curl (WSC) and wind-stress divergence, depending on the meteorological conditions and the ocean state. (For a demonstration of these distinctions in a global ocean general circulation model study see Milliff *et al.*, 1999.) Distributions of the scalar surface WSC are easiest to display graphically so we will focus our discussion on this derivative of the SVW process. The concepts of time- and space-dependent localization of uncertainty apply to vector winds, wind stresses and wind-stress divergence as well.

The surface WSC is a source of momentum and vorticity for the upper ocean. WSC drives Ekman pumping and suction on mesoscale space- and time-scales, affecting a multivariate response in the upper ocean (i.e. horizontal and vertical velocities, sea-surface height, SST, etc.). The WSC field derives from spatial derivatives of the surface wind-stress vector field (Milliff and Morzel, 2001). Subtle differences in the SVW can lead to large differences in WSC. This is because the drag law used to derive stress vectors from SVW goes as the square or cube of the SVW (Large *et al.*, 1994), and because the curl is a spatial derivative that can also exacerbate differences between SVW realizations.

Figure 7 documents the evolution of the WSC field for 1 February 2005 (day 8*A*) at midnight, 0600, noon and 1800 UTC (from top to bottom). The left-hand column depicts the posterior mean WSC summary from the BHM–SVW, and the right-hand column demonstrates the spread in WSC as computed from 10 realizations selected from the BHM–SVW posterior distribution. The 24 h evolution in Figure 7 is typical. For this day, a Mistral event generates the largest amplitude (positive and negative) WSC signals in the domain at midnight UTC (left column, top). The largest amplitude standard deviations are associated with this event as well (right column, top). However, while the WSC event is an atmospheric synoptic-scale feature, the signals in the standard deviation field exhibit an ocean mesoscale variability. Similar distinctions in scale. i.e. WSC mean versus WSC standard deviation, are evident at all times in Figure 7.

Milliff and Morzel (2001) demonstrate that time-dependent amplitude variations in WSC are much larger than for the SVW. Figure 7 demonstrates this for the Mediterranean Sea for the 1 day sequence of 4 snaphsots shown. Moreover, Figure 7 (right column) also shows that the uncertainty in WSC is highly variable in space and time. The Mistral signal at midnight strengthens by 0600 UTC. A weaker overall synoptic WSC picture is evident at noon, but relatively large-amplitude WSC standard deviations appear in the eastern Ionian Sea at this time. The atmospheric synoptic-scale picture strengthens in the eastern basin at 1800 UTC, as do the large-amplitude oceanic mesoscale WSC standard deviations. Therefore, the largest amplitude WSC standard deviation signals at the ocean mesoscale are predominantly associated with the largest amplitude mean WSC events on atmospheric synoptic scales. Both WSC and WSC standard deviations are highly variable in space and time.

The highly variable WSC uncertainties in space and time contribute to distributions of ocean state-variable uncertainties with amplitude peaks at mesoscale resolution as well. From an ensemble initial-condition generation perspective, this is a desirable property. The uncertainty in the ocean state will be preferentially driven, time step by time step, in association with the largest forcing events in the Mediterranean domain, wherever they are observed. Further, while the forcing events are of atmospheric synoptic scale, the ocean forcing uncertainty associated with them occurs on oceanic mesoscales. As a result, the most uncertain part of the ocean forecast (i.e. the ocean mesoscale) is the scale at which the ensemble spreads are the largest at any given time.

The ensemble initial-condition spreads in SST and SSH will be used to demonstrate multivariate ocean-state response to BHM–SVW spread in the following.

Figure 8 presents the ensemble mean SST (top panel) and ensemble standard deviation (bottom panel) for SST at the ensemble forecast initial-condition time (i.e. day 14*A* at 1200 UTC). The ensemble spread localizes in a few regions where ocean response to ensemble forcing is large. In addition, a background ocean mesoscale signal is more widespread, with specific regional maxima that coincide with variable regions of the Mediterranean Sea general circulation.

The posterior mean SST at day 14*A* (Figure 8, top) exhibits large-scale patterns including cooler northern and western SSTs and warmer southern and eastern basin SSTs. Some features of the general circulation of the Mediterranean Sea are evident as well. Large-scale cyclonic gyres (e.g. Gulf of Lyon Gyre centred at 5°E, 40°N; Rhodes Gyre centred at 28°E, 35°N) are marked by relatively cool SST patterns that are coherent on regional scales. Relatively sharp SST spatial gradients denote current systems and permanent features of the Mediterranean general circulation (e.g. the Algerian current region of the western basin, the Mersa Matruh Gyre at 27°E, 32°N, etc.). Signals of strong air–sea heat-flux interactions are also evident (e.g. the northernmost regions of the Adriatic Sea). A vigorous mesoscale variability is superposed on the large-scale patterns in the posterior mean SST as well.

In contrast, the SST standard deviation map (Figure 8, bottom) is dominated by ocean mesoscale signals only. Moreover, the spread is not uniformly distributed in space, but rather is localized, associated with specific oceanic responses to the space–time distribution of the surface wind.

Figure 9 is the ensemble mean and ensemble standard deviation for the sea-surface height (SSH) in a format

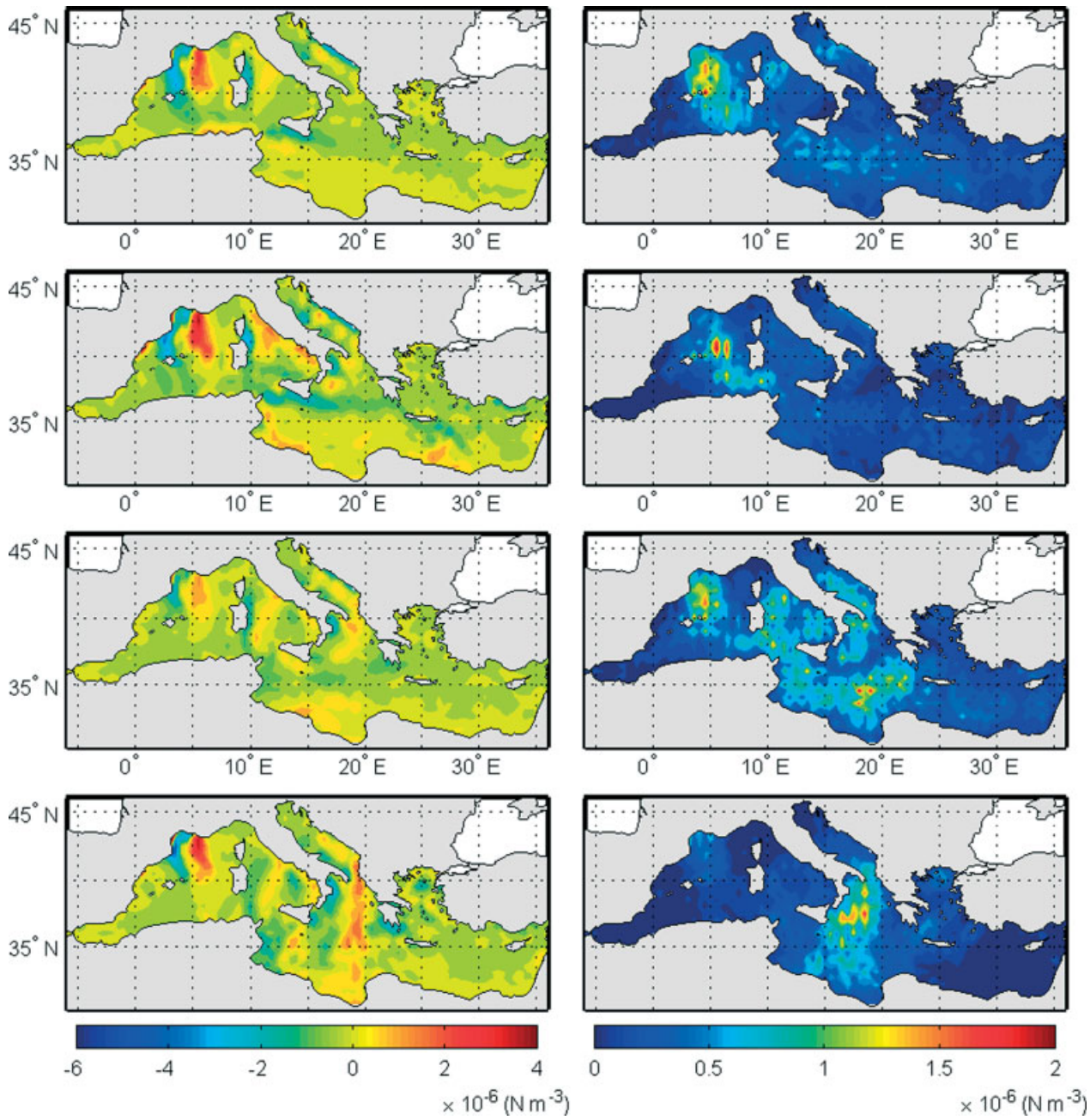

Figure 7. Wind-stress curl maps for four canonical times (0000, 0600, 1200 and 1800 UTC from top to bottom) on 1 February 2005 (day 8*A*) from the posterior distribution of the BHM–SVW. The left column is the posterior mean WSC for each time and the right column maps are the standard deviations in WSC as computed from 10 realizations of the posterior distribution (note change in colour bars). The WSC uncertainty is amplified in mesoscale features that occur in the vicinity of large-amplitude WSC events on synoptic scales.

identical to Figure 8 for SST. Similarities in locations and relative maxima with respect to Figure 8 support the notion that realistic spread in the SVW posterior distribution is driving multivariate responses in the ocean initial states.

As was the case for SST (Figure 8), the SSH posterior mean field (Figure 9, top) depicts features of the ocean general circulation and ocean synoptic-scale variability of the Mediterranean Sea, with an overlay of ocean mesoscale variability in specific regions. The eastward meandering flows of the Algerian Current, the Atlantic–Ionian Stream and the alongshore flow off the northern coast of Africa in the eastern basin are all evident* (Figure 9, top). Similarly, large-scale cyclonic circulations are implied in the Gulf of Lyon, the northern Ionian Sea and the Rhodes Gyre region. The Mersa Matruh Gyre is a large-amplitude positive SSH signal in the southern Levantine Sea.

The SSH standard-deviation field (Figure 9, bottom) exhibits its largest spreads in the vicinities of (1) a synoptic eddy formation event in the Algerian Current at 6°E, 37–38°N, (2) a northward-penetrating tight-radius meander of the Atlantic–Ionian Stream at 15°E, 35°N and (3) the coastal current between 20°E and 25°E, upstream of the Mersa Matruh Gyre. These loci were also evident in the

*Surface currents in Figure 9 are inferred by gradients between relatively high SSH (reds, generally to the south) and relatively low SSH (blues, generally to the north). The implied flow is along SSH contours, directed such that high SSH lies to the right of the flow.

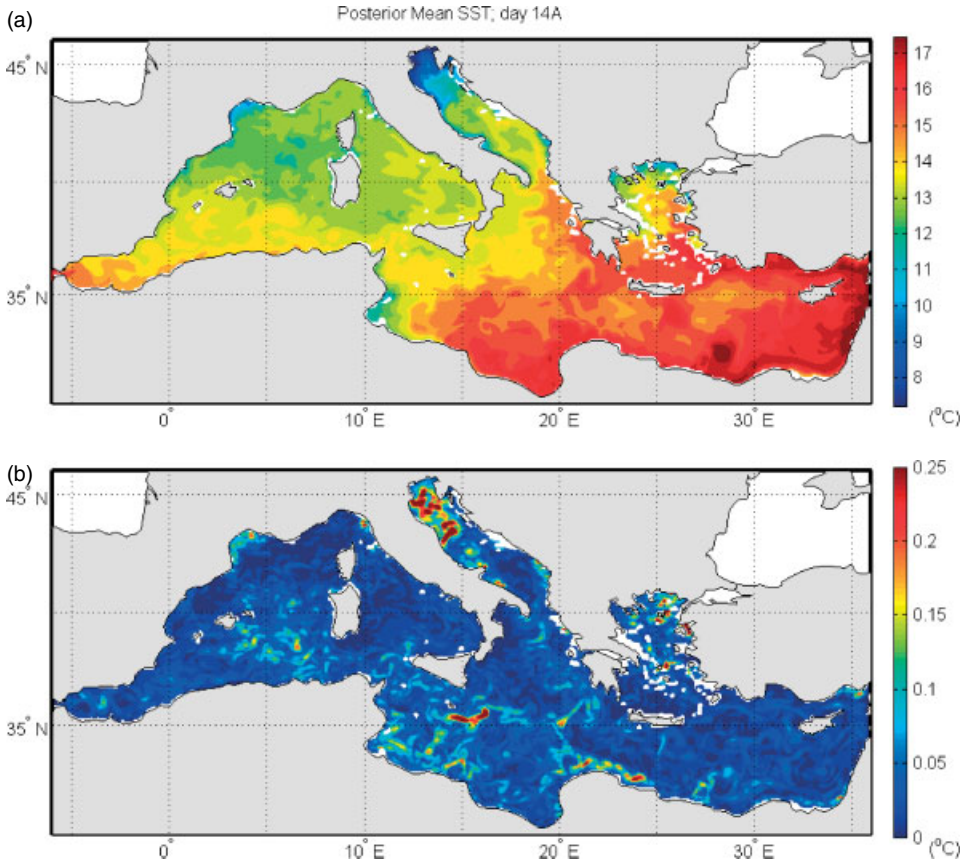

Figure 8. Sea-surface temperature (SST) posterior mean field (top panel) at noon on day 14*A*, i.e. the ensemble mean ocean forecast initial condition. SST standard deviation over 10 realizations from the posterior distribution at the initial condition time is in the bottom panel. The standard deviation in initial condition SST (bottom panel) is a measure of the ensemble spread (i.e. uncertainty) in this field. The largest amplitude standard deviations occur in a few locations associated with eddy formation and instabilities in synoptic-scale currents, i.e. in the Algerian current, the Atlantic–Ionian Stream and on the north coast of Africa in the eastern basin, upstream of the Mersa Matruh Gyre. Also, SST spreads are large in the far northern Adriatic and Aegean Seas, probably due to air–sea heat exchanges in these regions.

SST standard-deviation map (Figure 8, bottom), indicating that the spread in the BHM–SVW posterior distribution is driving ensemble initial-condition spread in multivariate ocean fields. Because the sequential assimilation system is dynamically balanced, each ensemble member contributing to the multivariate spread evident in Figures 8 and 9 will be balanced as well.

Finally we note that there are ocean processes, important on MFS forecast time-scales, that are not directly affected by the wind forcing during an assimilation cycle. These processes should also be perturbed in proportion to observational and dynamical uncertainty in ensemble initial conditions (e.g. subthermocline density anomalies due to internal waves and/or past formation events, surface and subsurface inertial jets as in the Gibraltar regime, bottom-water flows, etc.). As such, the BHM–SVW provides a proof-of-concept regarding the utility of the BHM methodology for efficient ocean ensemble initial-condition generation and forcing for ensemble ocean forecasts. Applications of BHM remain to be devised to generate ensemble initial conditions efficiently for processes that are not dominantly wind-driven on MFS forecast time-scales.

6. Conclusions

The development of an ensemble ocean forecast capability for MFS requires methods for generating ensemble initial conditions and uniquely forcing ensemble members during the forecasts. To serve these purposes, the BHM methodology has been applied in a probabilistic model for the SVW to manage and exploit realistic uncertainties in observations and approximate physics. Perturbations of the SVW are appropriate for ensemble ocean forecast applications because the analysis error-growth time-scales are longer than in the atmosphere, and forecast errors are associated with adiabatic processes that are very often wind-driven. The BHM–SVW is a sensible approach given (1) abundant observations with well-known error properties, (2) well-known approximate dynamical models that match well with the available data and (3) the guarantee of balanced, multivariate responses in the ocean initial states comprising the ensemble initial conditions.

The spread computed from realizations of the SVW posterior distribution exhibits localized uncertainty in specific regions, and during events that are the large-amplitude wind drivers of the system for each time step. The resulting ocean initial-condition ensemble has realistic and useful spread where the wind-driven response is large and likely to have the largest impacts on the MFS forecast. The most uncertain component of the MFS ocean model response is the ocean mesoscale. This is the scale at which the spread in the realizations of the posterior mean from the BHM–SVW are amplified. The benefits to the ocean forecast of the BHM–SVW generated ensemble initial conditions and ensemble wind forcing are explored in a companion article (Part 2).

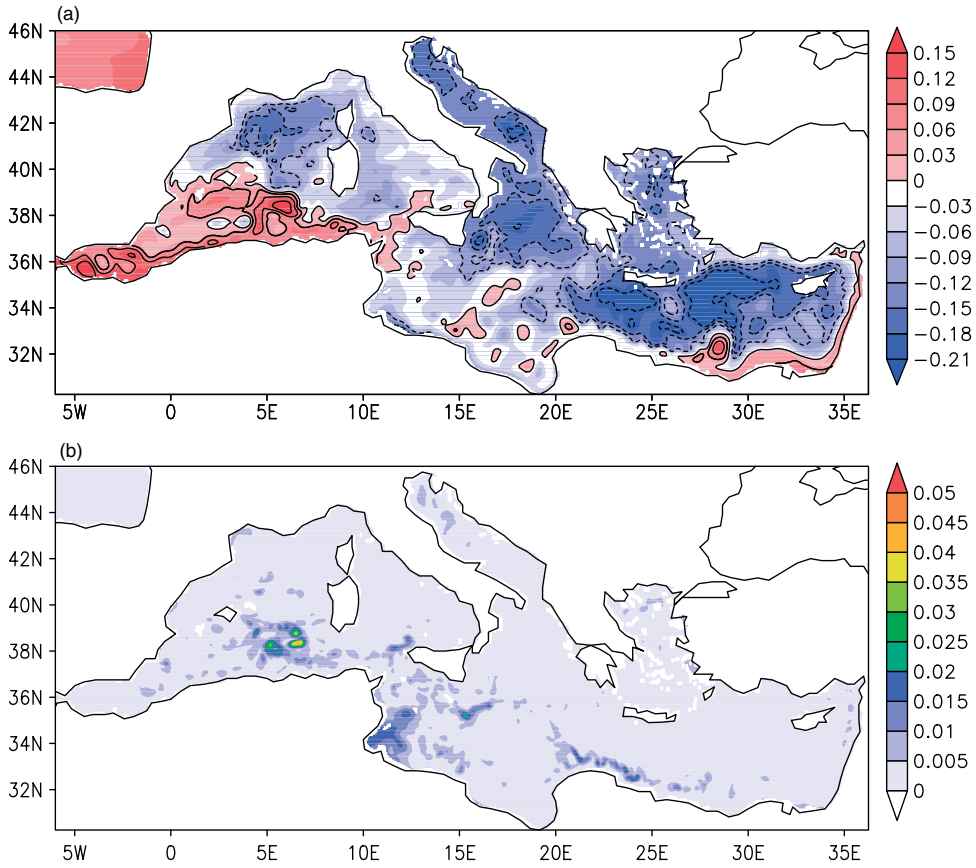

Figure 9. As in Figure 8 but for sea-surface height (SSH). The posterior mean SSH field at noon on day 14*A* is in the top panel and the standard deviation SSH computed over 10 realizations drawn from the posterior distribution on day 14*A* at noon is shown in the bottom panel. The standard deviation in initial-condition SSH is a measure of the ensemble spread (i.e. uncertainty) in this field. Uncertainty concentrates in mesoscale eddy structures, in the specific locations associated with instabilities in the synoptic-scale currents (i.e. the Algerian Current, the Atlantic–Ionian Stream and along the North African coast, just upstream of the Mersah Matruh Gyre).

Procedures to validate the BHM–SVW model development choices (e.g. what terms to make explicit in the process model, the sophistication of the data-stage error terms, etc.) are being developed. Many sensitivity tests remain to be designed and carried out. A sensitivity test reported here involved the inclusion/exclusion of QuikSCAT data in the data-stage distribution. The model is shown to be sensitive to these data in that inclusion of QuikSCAT data drives the modes of posterior distributions for the model parameters further from a simple geostrophic–ageostrophic interpretation of the SVW process, and it increases uncertainty in model parameters relative to the case that included only ECMWF data-stage inputs. This is presumably because the QuikSCAT data resolve time-dependent processes associated with low-pressure system development, frontal dynamics, etc. These processes occur on scales that correspond to large KE deficiencies in the data-stage inputs from ECMWF analyses. This suggests that BHM provides an efficient method for making better use of the high-resolution, but intermittent (in space and time) information content of modern earth-observing satellite systems.

The BHM–SVW development represents the latest step in adapting BHM to large state-space systems with relatively abundant, multiplatform observations and process models motivated by geophysical fluid dynamics. We have demonstrated that the BHM methodology is viable in the operational ensemble ocean forecast setting.

Postscript

Soon after this article was submitted, the QuikSCAT mission came to an end with the failure of the antenna system on the spacecraft. Since the demise of QuikSCAT, the Advanced Scatterometer (ASCAT) mission of the European operational satellite system (EUMETSAT) is the sole scatterometer system in operation, providing accurate SVW data at about 25 km resolution, in two swathes of about 512 km width, on either side of the subsatellite ground track (EUMETSAT, 2010). International efforts are under way to replace the QuikSCAT capability (Bourassa *et al.*, 2010; Chelton and Xie, 2010). It is also the case that numerical weather prediction (NWP) systems are continuously being upgraded to higher resolution in efforts to increase accuracies at finer spatial scales.[†]

The probabilistic properties of BHM–SVW ensure its relevance as NWP resolutions increase and SVW satellite systems evolve. BHM–SVW provides a realistic *distribution* of the SVW, from which realizations can be selected and used to drive ocean data assimilation and forecast integrations. Each SVW field realization from BHM–SVW is constrained to be reflective of the data (including any available scatterometer observations) and the process model, with realistic scatter according to the prescribed levels of uncertainty. The scatterometer data from QuikSCAT

[†]see http://www.ecmwf.int/products/changes/horizontal_resolution_2009.

added strength to BHM–SVW given their abundance and precision. Scatterometer data from ASCAT, while less abundant, will provide necessary information on mesoscale properties of the SVW, and these will be reflected in BHM–SVW applications based on these data. It remains to be seen what impacts recent increases in forecast-model resolution at ECMWF will have on SVW velocity variance. In addition to the forecast-model resolution, forecast-model parametrizations of surface boundary-layer processes have large effects on the SVW fields. Also, while forecast-model resolution increases, the resolutions of analysis and ensemble forecast products lag behind. BHM SVW realizations provide sufficient resolution to resolve important forcing events in the Mediterranean, such that the ocean forecast system responds with initial-condition uncertainty on the ocean mesoscale, which, appropriately, is the least certain component of the MFS.

Acknowledgements

This work has been funded by the Office of Naval Research, Physical Oceanography Program with grants and contracts to the Ohio State University (Berliner), the University of Missouri (Wikle) and NWRA/CoRA (Milliff). We thank our program manager Dr Manuel Fiadeiro for advice and interest in our program. The *in-kind* support of MFS scientists and supercomputing resources from INGV, Bologna have been essential to our effort, and are gratefully acknowledged. We appreciate inputs and operational perspectives from Drs Gregg Jacobs, Emanuel Coelho and James Richman of the Naval Research Laboratory, Stennis Space Center. We thank Professors Andrew Moore and Emanuele DiLorenzo and Dr Srdjan Dobricic for their inputs throughout the course of this work. R. F. Milliff also acknowledges additional support from NASA Ocean Vector Winds Science Team funding. Mr Jan Morzel and Dr Jeremiah Brown assisted with figure preparations. Constructive comments from two reviewers contributed to substantial improvements in the article.

A. BHM–SVW derivation

We begin by restating the full BHM–SVW, and follow with the full conditional distribution expressions for the random variables and parameters. Prior parameter specifications are provided in Appendix B. Bold letters indicate vectors and non-bold capital letters are assumed to be matrices, unless noted otherwise (e.g. $\mathbf{I}$ and Φ correspond to matrices).

A.1. BHM–SVW

The data-stage models for zonal and meridional wind components from scatterometer and ECMWF analyses and the data-stage model for SLP from ECMWF are

$$\begin{aligned}
\mathbf{D}^{s}_{u,t}|\mathbf{U}_t,\sigma^2_{\mathrm{s}} &\sim N(\mathbf{K}^{\mathrm{s}}_t\mathbf{U}_t,\sigma^2_{\mathrm{s}}\mathbf{I}),\\
\mathbf{D}^{s}_{v,t}|\mathbf{V}_t,\sigma^2_{\mathrm{s}} &\sim N(\mathbf{K}^{\mathrm{s}}_t\mathbf{V}_t,\sigma^2_{\mathrm{s}}\mathbf{I}),\\
\mathbf{D}^{\mathrm{e}}_{u,t}|\mathbf{U}_t,\sigma^2_{\mathrm{e}} &\sim N(\mathbf{K}^{\mathrm{e}}\mathbf{U}_t,\sigma^2_{\mathrm{e}}\mathbf{I}),\\
\mathbf{D}^{\mathrm{e}}_{v,t}|\mathbf{V}_t,\sigma^2_{\mathrm{e}} &\sim N(\mathbf{K}^{\mathrm{e}}\mathbf{V}_t,\sigma^2_{\mathrm{e}}\mathbf{I}),\\
\mathbf{D}^{\mathrm{e}}_{p,t}|\mu_p,\boldsymbol{\alpha}_t,\sigma^2_{ep} &\sim N(\mathbf{K}^{\mathrm{e}}(\mu_p\mathbf{1}+\Phi\boldsymbol{\alpha}_t),\sigma^2_{ep}\mathbf{I}),
\end{aligned}$$

where $\mathbf{I}$ is an identity matrix and $\mathbf{1}$ is a vector of 1s. The process models for $\mathbf{U}_t$, $\mathbf{V}_t$ are

$$\begin{aligned}
&\mathbf{U}_t|\mathbf{P}_t,a_{1,1},a_{1,2},\boldsymbol{\beta}^u_t,\sigma^2_u\\
&\qquad\sim N(a_{1,1}\mathbf{D}_y\mathbf{P}_t+a_{1,2}\mathbf{D}_x\mathbf{P}_t+\boldsymbol{W}\boldsymbol{\beta}^u_t,\sigma^2_u\mathbf{I}),\\
&\mathbf{V}_t|\mathbf{P}_t,b_{1,1},b_{1,2},\boldsymbol{\beta}^v_t,\sigma^2_v\\
&\qquad\sim N(b_{1,1}\mathbf{D}_x\mathbf{P}_t+b_{1,2}\mathbf{D}_y\mathbf{P}_t+\boldsymbol{W}\boldsymbol{\beta}^v_t,\sigma^2_v\mathbf{I}).
\end{aligned}$$

Since $\mathbf{P}_t=\mu_p\mathbf{1}+\Phi\boldsymbol{\alpha}_t$, the process model for $\boldsymbol{\alpha}_t$ is given by

$$\begin{aligned}
\boldsymbol{\alpha}_t &\sim N(\mathbf{0},\Lambda),\quad \Lambda\equiv\mathrm{diag}(\boldsymbol{\lambda}),\\
&\boldsymbol{\lambda}=(\lambda_1,\lambda_2,\ldots,\lambda_m)'.
\end{aligned}$$

At the next (parameter) level of the model hierarchy we have:

$$\begin{aligned}
a_{1,j} &\sim N(\mu_{a_{1,j}},\sigma^2_{a_{1,j}}),\\
b_{1,j} &\sim N(\mu_{b_{1,j}},\sigma^2_{b_{1,j}}),\ j=1,2;\\
\lambda_i &\sim IG(q_i,r_i),\ i=1,\ldots,m,
\end{aligned}$$

where *IG* indicates an inverse gamma distribution.

The distributions for the $\boldsymbol{\beta}^u_t$, $\boldsymbol{\beta}^v_t$ weights for the wavelet basis terms are given by

$$\begin{aligned}
\boldsymbol{\beta}^u_t|\mathbf{M}_u,\boldsymbol{\beta}^u_{t-1} &\sim N(\mathbf{M}_u\boldsymbol{\beta}^u_{t-1},\Sigma_{\beta u}),\\
\boldsymbol{\beta}^v_t|\mathbf{M}_v,\boldsymbol{\beta}^v_{t-1} &\sim N(\mathbf{M}_v\boldsymbol{\beta}^v_{t-1},\Sigma_{\beta v}),
\end{aligned}$$

where $\mathbf{M}_u\equiv\mathrm{diag}(\mathbf{m}_u)$, $\mathbf{m}_u=(m_u(1),\ldots,m_u(n_\beta))'$ and $\Sigma_{\beta u}\equiv\mathrm{diag}(\sigma^2_{\beta u}(1),\ldots,\sigma^2_{\beta u}(n_\beta))$. Similar expressions apply to $\mathbf{M}_v$, $\mathbf{m}_v$ and $\Sigma_{\beta v}$. At $t=0$, $\boldsymbol{\beta}^u_0\sim N(\boldsymbol{\mu}_{u_0},\Sigma_{u_0})$ and $\boldsymbol{\beta}^v_0\sim N(\boldsymbol{\mu}_{v_0},\Sigma_{v_0})$.

Finally, we have

$$\begin{aligned}
\mathbf{m}_u &\sim N(\boldsymbol{\mu}_{mu},\Sigma_{mu}),\\
\Sigma_{mu} &= \mathrm{diag}(\sigma^2_{mu}(1),\ldots,\sigma^2_{mu}(n_\beta)),\\
\mathbf{m}_v &\sim N(\boldsymbol{\mu}_{mv},\Sigma_{mv}),\\
\Sigma_{mv} &= \mathrm{diag}(\sigma^2_{mv}(1),\ldots,\sigma^2_{mv}(n_\beta)),\\
\sigma^2_{\beta u}(i) &\sim IG(q_{\beta u}(i),r_{\beta u}(i)),\\
\sigma^2_{\beta v}(i) &\sim IG(q_{\beta v}(i),r_{\beta v}(i)),\\
\sigma^2_u &\sim IG(q_u,r_u),\\
\sigma^2_v &\sim IG(q_v,r_v).
\end{aligned}$$

A.2. Full conditional distributions

The Gibbs Sampler algorithm generates, in sequence, samples of the random variables and parameters of the process model and data stage for $\mathcal{O}(10^4)$ iterations. Values for variables and parameters are used as soon as they are sampled *within* each iteration. In the following, we outline the sequence of full conditional distributions in the order that they occur within our Gibbs Sampler for BHM–SVW. Let $\mathbf{H}_u=a_{1,1}\mathbf{D}_y+a_{1,2}\mathbf{D}_x$ and $\mathbf{H}_v=b_{1,1}\mathbf{D}_y+b_{1,2}\mathbf{D}_x$, where $\mathbf{D}_x$ and $\mathbf{D}_y$ are first-order spatial difference operator matrices.

The full conditional distributions for the zonal velocity $\mathbf{U}_t$, $t = 1, \ldots, T$ are

$$
\begin{aligned}
&[\mathbf{U}_t|\cdot] \\
&\propto [\mathbf{D}^{\mathrm{s}}_{u,t}|\mathbf{U}_t, \sigma^2_{\mathrm{s}}]\,[\mathbf{D}^{\mathrm{e}}_{u,t}|\mathbf{U}_t, \sigma^2_{\mathrm{e}}]\,[\mathbf{U}_t|\mathbf{P}_t, \mathbf{H}_u, \boldsymbol{\beta}^u_t, \sigma^2_u\,] \\
&\quad \propto \exp\left\{-\frac{1}{2}\left[\frac{(\mathbf{D}^{\mathrm{s}}_{u,t} - \mathbf{K}^{\mathrm{s}}_t\mathbf{U}_t)'(\mathbf{D}^{\mathrm{s}}_{u,t} - \mathbf{K}^{\mathrm{s}}_t\mathbf{U}_t)}{\sigma^2_{\mathrm{s}}}\right.\right. \\
&\quad + \frac{(\mathbf{D}^{\mathrm{e}}_{u,t} - \mathbf{K}^{\mathrm{e}}\mathbf{U}_t)'(\mathbf{D}^{\mathrm{e}}_{u,t} - \mathbf{K}^{\mathrm{e}}\mathbf{U}_t)}{\sigma^2_{\mathrm{e}}} \\
&\quad \left.\left. + \frac{(\mathbf{U}_t - \mathbf{H}_u\mathbf{P}_t - \boldsymbol{W}\boldsymbol{\beta}^u_t)'(\mathbf{U}_t - \mathbf{H}_u\mathbf{P}_t - \boldsymbol{W}\boldsymbol{\beta}^u_t)}{\sigma^2_u}\right]\right\}.
\end{aligned}
\tag{A1}
$$

It can be shown that $\mathbf{U}_t|\cdot \sim N(\mathbf{A}\boldsymbol{b}, \mathbf{A})$, where

$$
\begin{aligned}
\mathbf{A} &= \left[\frac{\mathbf{K}^{\mathrm{s}\prime}_t\mathbf{K}^{\mathrm{s}}_t}{\sigma^2_{\mathrm{s}}} + \frac{\mathbf{K}^{\mathrm{e}\prime}\mathbf{K}^{\mathrm{e}}}{\sigma^2_{\mathrm{e}}} + \frac{\mathbf{I}}{\sigma^2_u}\right]^{-1}, \\
\boldsymbol{b} &= \left[\frac{\mathbf{D}^{\mathrm{s}}_{u,t}{}'\mathbf{K}^{\mathrm{s}}_t}{\sigma^2_{\mathrm{s}}} + \frac{\mathbf{D}^{\mathrm{e}\prime}_{u,t}\mathbf{K}^{\mathrm{e}}}{\sigma^2_{\mathrm{e}}} + \frac{(\mathbf{H}_u\mathbf{P}_t + \boldsymbol{W}\boldsymbol{\beta}^u_t)'}{\sigma^2_u}\right]'.
\end{aligned}
$$

Note that for the forecast times ($t = T, \ldots, T + \tau$) there are no satellite observations available. Hence, the resulting full conditional distributions are as above, with the exceptions that (1) the first terms in the expressions for $\mathbf{A}$ and $\mathbf{b}$ are removed and (2) the analysis winds in $\mathbf{D}^{\mathrm{e}}_{u,t}$ are replaced with ECMWF forecast winds.

Analogous expressions and assumptions describe the full conditional distribution for $\mathbf{V}_t$.

The SLP structure function weights are $\boldsymbol{\alpha}_t$, and their full conditional distributions ($t = 1, \ldots, T + \tau$) are given by

$$
\begin{aligned}
&[\boldsymbol{\alpha}_t|\cdot] \\
&\propto [\mathbf{D}^{\mathrm{e}}_{p,t}|\boldsymbol{\alpha}_t, \sigma^2_{\mathrm{e}p}]\,[\mathbf{u}_t|\mathbf{H}_u, \boldsymbol{\alpha}_t, \boldsymbol{\beta}^u_t, \sigma^2_u] \\
&\quad \times [\mathbf{v}_t|\mathbf{H}_v, \boldsymbol{\alpha}_t, \boldsymbol{\beta}^v_t, \sigma^2_v]\,[\boldsymbol{\alpha}_t|\boldsymbol{\Lambda}]
\end{aligned}
$$

$$
\begin{aligned}
&\propto \exp\left\{-\frac{1}{2}\left[\frac{\{\mathbf{D}^{\mathrm{e}}_{p,t} - \mathbf{K}^{\mathrm{e}}(\mu_p\mathbf{1} + \Phi\boldsymbol{\alpha}_t)\}'}{\sigma^2_{\mathrm{e}p}}\right.\right. \\
&\quad \times \frac{\{\mathbf{D}^{\mathrm{e}}_{p,t} - \mathbf{K}^{\mathrm{e}}(\mu_p\mathbf{1} + \Phi\boldsymbol{\alpha}_t)\}}{\sigma^2_{\mathrm{e}p}} \\
&\quad \times \frac{\{\mathbf{U}_t - \mathbf{H}_u(\mu_p\mathbf{1} + \Phi\boldsymbol{\alpha}_t) - \boldsymbol{W}\boldsymbol{\beta}^u_t\}'}{\sigma^2_u} \\
&\quad \times \frac{\{\mathbf{U}_t - \mathbf{H}_u(\mu_p\mathbf{1} + \Phi\boldsymbol{\alpha}_t) - \boldsymbol{W}\boldsymbol{\beta}^u_t\}}{\sigma^2_u} \\
&\quad \times \frac{\{\mathbf{V}_t - \mathbf{H}_v(\mu_p\mathbf{1} + \Phi\boldsymbol{\alpha}_t) - \boldsymbol{W}\boldsymbol{\beta}^v_t\}'}{\sigma^2_v} \\
&\quad \times \frac{\{\mathbf{V}_t - \mathbf{H}_v(\mu_p\mathbf{1} + \Phi\boldsymbol{\alpha}_t) - \boldsymbol{W}\boldsymbol{\beta}^v_t\}}{\sigma^2_v} \\
&\quad \left.\left. \times \boldsymbol{\alpha}_t{}'\Lambda^{-1}\boldsymbol{\alpha}_t\right]\right\},
\end{aligned}
$$

which implies that $[\boldsymbol{\alpha}_t|\cdot] \propto [\boldsymbol{D}^e_{p,t}|\boldsymbol{\alpha}_t, \sigma^2_{ep}]$, where

$$
\begin{aligned}
\mathbf{A} = \left[\frac{\Phi'\mathbf{K}^{\mathrm{e}\prime}\mathbf{K}^{\mathrm{e}}\Phi}{\sigma^2_{ep}} + \frac{(\Phi'\mathbf{H}'_u\mathbf{H}_u\Phi)}{\sigma^2_u}\right. \\
\left. + \frac{(\Phi'\mathbf{H}'_v\mathbf{H}_v\Phi)}{\sigma^2_v} + \boldsymbol{\Lambda}^{-1}\right]^{-1},
\end{aligned}
$$

$$
\begin{aligned}
\boldsymbol{b} = \left[\frac{(\mathbf{D}^{\mathrm{e}}_{p,t} - \mathbf{K}^{\mathrm{e}}\mathbf{1}\mu_p)'\mathbf{K}^{\mathrm{e}}\Phi}{\sigma^2_{ep}}\right. \\
+ \frac{(\mathbf{U}_t - \mathbf{H}_u\mathbf{1}\mu_p - \boldsymbol{W}\boldsymbol{\beta}^u_t)'\mathbf{H}_u\Phi}{\sigma^2_u} \\
\left. + \frac{(\mathbf{V}_t - \mathbf{H}_v\mathbf{1}\mu_p - \boldsymbol{W}\boldsymbol{\beta}^v_t)'\mathbf{H}_v\Phi}{\sigma^2_v}\right]'.
\end{aligned}
$$

In this case, Λ is a diagonal matrix with parameters λ_i on the diagonal. The full conditional distributions for λ_i are given by

$$
[\lambda_i|\cdot] \propto \prod_{t=1}^{T+\tau} [\alpha_{i,t}|\lambda_i][\lambda_i]
$$

and

$$
\lambda_i \sim IG\left(q_i + \frac{T+\tau}{2}, \left[\frac{1}{r_i} + \frac{1}{2}\sum_{t=1}^{T}\alpha^2_{i,t}\right]^{-1}\right).
$$

The full conditional distributions for the wavelet coefficients $\boldsymbol{\beta}^u_t$ are given by

$$
[\boldsymbol{\beta}^u_t|\cdot] \propto [\mathbf{U}_t|\mathbf{H}_u, \mathbf{P}_t, \boldsymbol{\beta}^u_t, \sigma^2_u][\boldsymbol{\beta}^u_t|\boldsymbol{\beta}^u_{t-1}][\boldsymbol{\beta}^u_{t+1}|\boldsymbol{\beta}^u_t]
$$

for $t = 1, \ldots, T + \tau - 1$. Expanding,

$$
\begin{aligned}
[\boldsymbol{\beta}^u_t|\cdot] \propto \exp\left\{-\frac{1}{2}\left[\frac{(\mathbf{U}_t - \mathbf{H}_u\mathbf{P}_t - \boldsymbol{W}\boldsymbol{\beta}^u_t)'}{\sigma^2_u}\right.\right. \\
\times \frac{(\mathbf{U}_t - \mathbf{H}_u\mathbf{P}_t - \boldsymbol{W}\boldsymbol{\beta}^u_t)}{\sigma^2_u} \\
\times (\boldsymbol{\beta}^u_t - \mathbf{M}_u\boldsymbol{\beta}^u_{t-1})'\Sigma^{-1}_{\beta u}(\boldsymbol{\beta}^u_t - \mathbf{M}_u\boldsymbol{\beta}^u_{t-1}) \\
\left.\left. \times (\boldsymbol{\beta}^u_{t+1} - \mathbf{M}_u\boldsymbol{\beta}^u_t)'\Sigma^{-1}_{\beta u}(\boldsymbol{\beta}^u_{t+1} - \mathbf{M}_u\boldsymbol{\beta}^u_t)\right]\right\}.
\end{aligned}
$$

Thus, $\boldsymbol{\beta}^u_t|\cdot \sim N(\mathbf{A}\boldsymbol{b}, \mathbf{A})$, where

$$
\mathbf{A} = \left[\frac{\mathbf{I}}{\sigma^2_u} + {\Sigma_{\beta u}}^{-1} + \mathbf{M}_u{}'{\Sigma_{\beta u}}^{-1}\mathbf{M}_u\right]^{-1},
$$

$$
\begin{aligned}
\mathbf{b} = \left[\frac{(\mathbf{U}_t - \mathbf{H}_u\mathbf{P}_t)'\boldsymbol{W}}{\sigma^2_u}\right. \\
\left. + \boldsymbol{\beta}^u_{t-1}\mathbf{M}_u{}'{\Sigma_{\beta u}}^{-1} + \boldsymbol{\beta}^u_{t+1}{}'{\Sigma_{\beta u}}^{-1}\mathbf{M}_u\right]'.
\end{aligned}
$$

For $t = T + \tau$, $\boldsymbol{\beta}^u_{t+\tau}|\cdot \sim N(\mathbf{A}\mathbf{b}, \mathbf{A})$, where

$$
\mathbf{A} = \left[\frac{\mathbf{I}}{\sigma^2_u} + {\Sigma_{\beta u}}^{-1}\right]^{-1},
$$

$$
\mathbf{b} = \left[\frac{(\mathbf{U}_{T+\tau} - \mathbf{H}_u\mathbf{P}_{T+\tau})'\boldsymbol{W}}{\sigma^2_u} + \boldsymbol{\beta}^u_{T+\tau}{}'\mathbf{M}_u{}'{\Sigma_{\beta u}}^{-1}\right]'.
$$

For $t = 0$, $\boldsymbol{\beta}^u_0|\cdot \sim N(\mathbf{A}\mathbf{b}, \mathbf{A})$, where

$$
\begin{aligned}
\mathbf{A} &= \left[\mathbf{M}_u{}'{\Sigma_{\beta u}}^{-1}\mathbf{M}_u + {\Sigma_{u_0}}^{-1}\right]^{-1}, \\
\mathbf{b} &= \left[\boldsymbol{\beta}^{u\prime}_1{\Sigma_{\beta u}}^{-1}\mathbf{M}_u + \boldsymbol{\mu}_{u_0}{}'{\Sigma_{u_0}}^{-1}\right]'.
\end{aligned}
$$

Analogous expressions and assumptions describe the full conditional distributions for $\boldsymbol{\beta}_t^v, t = 0, \ldots, T+\tau$.

The full conditional distributions for the autoregressive parameters $\mathbf{m}_u$ are given by

$$[\mathbf{m}_u|\cdot] \propto \prod_{t=1}^{T+\tau} [\boldsymbol{\beta}_t^u|\boldsymbol{\beta}_{t-1}^u, \mathbf{m}_u, \Sigma_{\beta u}][\mathbf{m}_u],$$

where $\Sigma_{\beta u}$ is diagonal with elements $\sigma_{\beta u}^2(i)$, $i = 1, \ldots, n_\beta$, and we define Σ_{mu} as diagonal with elements σ_{mu}^2. Then,

$$[m_u(i)|\cdot] \propto \prod_{t=1}^{T+\tau} [\beta_t^u(i)|\beta_{t-1}^u(i), m_u(i), \sigma_{\beta u}^2(i)][m_u(i)].$$

Thus, $m_u(i)|\cdot \sim N(ab, a)$, where

$$\begin{aligned} a &= \left[\frac{\sum_{t=1}^{T+\tau}(\beta_{t-1}^u(i))^2}{\sigma_{\beta u}^2(i)} + \frac{1}{\sigma_{mu}^2(i)}\right]^{-1}, \\ b &= \frac{\sum_{t=1}^{T+\tau} \beta_{t-1}^u(i)\beta_t^u(i)}{\sigma_{\beta u}^2(i)} + \frac{\mu_{mu}(i)}{\sigma_{mu}^2(i)}. \end{aligned}$$

Full conditional distributions for the elements of $\mathbf{m}_v$ are analogous to $\mathbf{m}_u$.

The full conditional distributions for the variance terms on the diagonal of $\Sigma_{\beta u}$ are given by

$$[\sigma_{\beta u}^2(i)|\cdot] \propto \prod_{t=1}^{T+\tau} [\beta_t^u(i)|\beta_{t-1}^u(i), m_u(i), \sigma_{\beta u}^2(i)][\sigma_{\beta u}^2(i)]$$

and

$$\sigma_{\beta u}^2(i)|\cdot \sim IG\Bigg(q_{\beta u}(i) + \frac{T+\tau}{2}, \left[\frac{1}{r_{\beta u}(i)} + \frac{1}{2}\sum_{t=1}^{T+\tau}(\beta_t^u(i) - m_u(i)\beta_{t-1}^u(i))^2\right]^{-1}\Bigg).$$

The full conditional distribution for $\sigma_{\beta v}^2(i)$ is analogous to $\sigma_{\beta u}^2(i)$.

The full conditional distribution for the zonal velocity variance term is

$$[\sigma_u^2|\cdot] \propto \prod_{t=1}^{T+\tau} [\mathbf{U}_t|\mathbf{P}_t, \mathbf{H}_u, \boldsymbol{\beta}_t^u, \sigma_u^2][\sigma_u^2]$$

and

$$\sigma_u^2|\cdot \sim IG\Bigg(q_u + \frac{n(T+\tau)}{2}, \Big[\frac{1}{r_u} + \frac{1}{2}\sum_{t=1}^{T+\tau}(\mathbf{U}_t - \mathbf{H}_u\mathbf{P}_t - \boldsymbol{W}\boldsymbol{\beta}_t^u)' \times (\mathbf{U}_t - \mathbf{H}_u\mathbf{P}_t - \boldsymbol{W}\boldsymbol{\beta}_t^u)\Big]^{-1}\Bigg).$$

The full conditional distribution for σ_v^2 is analogous to σ_u^2.

The full conditional distribution for the random coefficient $a_{1,1}$ is given by

$$[a_{1,1}|\cdot] \propto \prod_{t=1}^{T+\tau} [\mathbf{U}_t|\mathbf{P}_t, a_{1,1}, a_{1,2}, \boldsymbol{\beta}_t^u, \sigma_u^2][a_{1,1}].$$

Thus, $a_{1,1}|\cdot \sim N(ab, a)$, where

$$\begin{aligned} a &= \left[\sum_{t=1}^{T+\tau} \frac{(\mathbf{P}_t'\mathbf{D}_y'\mathbf{D}_y\mathbf{P}_t)}{\sigma_u^2} + \frac{1}{\sigma_{a_{1,1}}^2}\right]^{-1}, \\ b &= \sum_{t=1}^{T+\tau} \frac{(\mathbf{U}_t - a_{1,2}\mathbf{D}_x\mathbf{P}_t)'\mathbf{D}_y\mathbf{P}_t}{\sigma_u^2} + \frac{\mu_{a_{1,1}}}{\sigma_{a_{1,1}}^2}. \end{aligned}$$

Similarly, the full conditional distribution for $a_{1,2}$ is given by $a_{1,2}|\cdot \sim N(ab, a)$, where

$$\begin{aligned} a &= \left[\sum_{t=1}^{T+\tau} \frac{(\mathbf{P}_t'\mathbf{D}_x'\mathbf{D}_x\mathbf{P}_t)}{\sigma_u^2} + \frac{1}{\sigma_{a_{1,2}}^2}\right]^{-1}, \\ b &= \sum_{t=1}^{T+\tau} \frac{(\mathbf{U}_t - a_{1,1}\mathbf{D}_y\mathbf{P}_t)'\mathbf{D}_x\mathbf{P}_t}{\sigma_u^2} + \frac{\mu_{a_{1,2}}}{\sigma_{a_{1,2}}^2}. \end{aligned}$$

The full conditional distributions for $b_{1,1}$ and $b_{1,2}$ are analogous to those for $a_{1,1}$ and $a_{1,2}$.

B. Hyperprior specifications for the BHM–SVW

B.1. Data-stage parameters

$$\begin{aligned} \sigma_s^2 &= 1\,\mathrm{m^2\,s^{-2}}, \\ \sigma_e^2 &= 10\,\mathrm{m^2\,s^{-2}}, \\ \sigma_{ep}^2 &= 200\,\mathrm{hPa^2}. \end{aligned}$$

B.2. Process-model stage parameters

The parameters of the inverse Gamma distributions for $\sigma_{u,v}^2$ are

$$\begin{aligned} q_u &= q_v = 2.0025, \\ r_u &= r_v = 1.9950. \end{aligned}$$

These correspond to mean values of $0.5\,\mathrm{m^2\,s^{-2}}$ and variances of $100\,\mathrm{m^4\,s^{-4}}$. The λ_i IG parameters are

$$q_i = 1.000002 \times 10^6, \qquad r_i = 1 \times 10^{-13},$$

corresponding to mean value $10^7\,\mathrm{hPa^2}$ and variance $10^8\,\mathrm{hPa^4}$. The means and variances for the parameters of the Gaussian distributions for the process-model geostrophic–ageostrophic coefficients are

$$\begin{aligned} \mu_{a_{1,1}} &= -8690, & \sigma_{a_{1,1}}^2 &= 10^6, \\ \mu_{a_{1,2}} &= -4380, & \sigma_{a_{1,1}}^2 &= 10^6, \\ \mu_{b_{1,1}} &= -4380, & \sigma_{a_{1,1}}^2 &= 10^6, \\ \mu_{b_{1,2}} &= 8690, & \sigma_{a_{1,1}}^2 &= 10^6. \end{aligned}$$

Table B1. Parameters of IG distributions for $\sigma^2_{\beta u,v}$ at each spatial scale and the corresponding means and variances.

i	Scale	Mean	Var	$q_{\beta u,v}$	$r_{\beta u,v}$
1	L	192.0	0.0001	3.7×10^{8}	1.4×10^{-11}
2	M	24.0	1.0	5.8×10^{2}	7.2×10^{-5}
3	S	3.0	1.0	1.1×10^{1}	3.3×10^{-2}

The parameters for the mean and variance terms in the wavelet weights are

$$\begin{aligned} \mu_{mu}(i) &= \mu_{mv}(i) = 0.4, \\ \sigma^2_{mu} &= \sigma^2_{mv} = 0.01. \end{aligned}$$

Three scales of nested wavelets comprise the basis set used in the process-model term. The parameters of IG distributions for $\sigma^2_{\beta u,v}$, at each spatial scale (i.e. large, medium, small) and the corresponding means and variances are listed in Table B1.

Finally, the initial values for the mean and variance for $\boldsymbol{\beta}_0^{u,v}$ are $\boldsymbol{\mu}_{u_0,v_0} = \mathbf{0}$, and Σ_{u_0,v_0} is diagonal with variances for the three scales of resolution corresponding to the variance values in the table above.

References

Anderson CJ, Wikle CK, Zhou Q, Royle JA. 2007. Population influences on tornado reports in the United States. *Weather and Forecasting* **22**: 571–579.

Berliner LM. 2003. Physical–statistical modeling in Geophysics. *J. Geophys. Res.* **108**(D24): 8776. DOI:10.1029/2002JD002865.

Berliner LM, Kim Y. 2008. Bayesian design and analysis for superensemble-based climate forecasting. *J. Climate* **21**: 1891–1910.

Berliner LM, Milliff RF, Wikle CK. 2003. Bayesian hierarchical modelling of air–sea interaction. *J. Geophys. Res.* **108**(C4): 3104. DOI:10.1029/2002JC001413.

Bonazzi A. 2008. '*Ensemble Forecasting in the Mediterranean Sea*'. PhD Dissertation, University of Bologna, 156 pp.

Bourassa MA, Bonekamp H, Chang P, Chelton D, Courtney J, Edson R, Figa J, He Y, Hersbach H, Hilburn K, Jelenak Z, Lee T, Liu WT, Long D, Kelly K, Knabb R, Lindstorm E, Perrie W, Portabella M, Powell M, Rodriguez E, Smith D, Stoffelen A, Swail V, Wentz F. 2010. 'Remotely sensed winds and wind stresses for marine forecasting and ocean modeling'. In *Proceeding, OceanObs'09: Sustained Ocean Observations and Information for Society, Venice, Italy*. IOC/UNESCO and ESA. DOI:10.5270/OceanObs09.cwp.08.

Chelton DB, Freilich MH. 2005. Scatterometer-based assessment of 10-m wind analyses from the operational ECMWF and NCEP numerical weather prediction models. *Mon. Weather Rev.* **133**: 409–429.

Chelton DB, Xie S-P. 2010. Coupled ocean–atmosphere interactions at oceanic mesoscales. *Oceanogr. Magazine.* **23**: 52–69.

Chelton DB, Schlax MG, Freilich MH, Milliff RF. 2004. Satellite measurements reveal persistent small-scale features in ocean winds. *Science* **303**: 978–983.

Dobricic S, Pinardi N, Adani M, Bonazzi A, Fratianni D, Tonani M. 2005. Mediterranean Forecasting System: An improved assimilation scheme for sea level anomaly and its validation. *Q. J. R. Meteorol. Soc.* **131**: 3627–3642.

Dobricic S, Pinardi N, Adani M, Tonani M, Fratianni C, Bonazzi A, Fernandez V. 2007. Daily oceanographic analyses by the Mediterranean basin scale assimilation system. *Ocean Sci.* **3**: 149–157.

Draper DW, Long DG. 2002. An assessment of SeaWinds on QuikSCAT wind retrieval. *J. Geophys. Res.* **107**(C): 3212. DOI:10.1029/2002JC001330.

Ebuchi N, Graber HC, Caruso MJ. 2002. Evaluation of wind vectors observed by QuikSCAT/SeaWinds using ocean buoy data. *J. Atmos. Oceanic Technol.* **19**: 2049–2062.

Ehrendorfer M. 2007. A review of issues in ensemble-based Kalman filtering. *Meteorol. Zeitschrift* **16**(6): 795–818.

Ehrendorfer M. 2008. 'Review of issues concerning ensemble-based data assimilation techniques'. Presentation to *Banff International Research Station for Mathematical Innovation and Discovery (BIRS), Workshop on Mathematical Advancement in Geophysical Data Assimilation*, 3–8 February 2008. Copyright BIRS 2010. See also: www.atmos.ucla.edu/˜kayo/birs/pdf/ehrendorfer birs da08.pdf.

EUMETSAT Ocean and Sea Ice Satellite Applications Facility (OSI SAF). 2010. '*ASCAT Product User Manual, Version 1.8*', copyright EUMETSAT 2010. 24 pp.

Evensen G. 2003. The ensemble Kalman filter: Theoretical formulation and practical implementation. *Ocean Dyn.* **53**: 343–367.

Freilich MH. 1996. '*SeaWinds algorithm theoretical basis document*', 56 pp. NASA Jet Propulsion Laboratory, California Institute of Technology: Pasadena, CA. Available online at: http://podaac.jpl.nasa.gov/quikscat/qscat_doc.html.

Freilich MH. 1997. Validation of vector magnitude datasets: Effects of random component errors. *J. Atmos. Oceanic Technol.* **14**: 696–703.

Freilich MH, Vanhoff B. 2003. 'The accuracy of the QuikSCAT standard (L2B and DIRTH) wind products'. In *Proc. Ocean Vector Winds Science Team Meeting, Oxnard, CA*. NASA Jet Propulsion Laboratory, Pasadena, CA, USA.

Fox NI, Wikle CK. 2005. A Bayesian quantitative precipitation nowcast scheme. *Weather and Forecasting* **20**: 264–275.

Gilks WR. 1996. *Markov Chain Monte Carlo in practice*, Gilks WR, Richardson S, Spiegelhalter DJ (eds). Chapman Hall/CRC: London; pp 75–88.

Gilks WR, Richardson S, Spiegelhalter DJ. 1996. *Markov Chain Monte Carlo in practice*, Gilks WR, Richardson S, Spiegelhalter DJ (eds). Chapman Hall/CRC: London; pp 1–20.

Hoar TJ, Milliff RF, Wikle CK, Nychka D, Berliner LM. 2003. Winds from a Bayesian hierarchical model: Computation for atmosphere–ocean research. *J. Comput. Graphical Stat.* **12**: 781–807.

Kersale M, Doglioli AM, Petrenko AA. 2010. Sensitivity study of wind forcing in a numerical model of mesoscale eddies in the lee of Hawaii islands. *Ocean Sci. Discuss.* **7**: 477–500.

Large WG, McWilliams JC, Doney SM. 1994. Oceanic vertical mixing: A review and a model with a nonlocal boundary layer parameterization. *Rev. Geophys.* **32**: 363–403.

McWilliams JC, Brown ED, Bryden HL, Ebbesmeyer CC, Elliot BA, Heinmiller RH, Hua BL, Leaman KD, Lindstrom EJ, Luyten JR, McDowell SE, Owens WB, Perkins H, Price JF, Regier L, Riser SC, Rossby HT, Sanford TB, Shen CY, Taft BA, Van Leer JC. 1983. 'The local dynamics of eddies in the western North Atlantic'. In *Eddies in Marine Science*, Robinson AR (ed). Springer-Verlag: Berlin; pp 92–113.

Milliff RF, Large WG, Holland WR, McWilliams JC. 1996. The general circulation responses of high-resolution North Atlantic ocean models to synthetic scatterometer winds. *J. Phys. Oceanogr.* **26**: 1747–1768.

Milliff RF. 2004. '*Comparing the kinetic energy versus wavenumber in surface wind fields from ECMWF analyses and the NASA QuikSCAT scatterometer*', Report No. NWRA-CoRA-04-R272 to Istituto Nazionale di Geofisica e Vulcanologia, Bologna, Italy, 18 pp. Also available at INGV Bologna, ITALY http://www.bo.ingv.it/mfstep/WP3/scat.htm.

Milliff RF, Morzel J. 2001. The global distribution of the time-average wind-stress curl from NSCAT. *J. Atmos. Sci.* **58**(2): 109–131.

Milliff RF, Large WG, Morzel J, Danabasoglu G, Chin TM. 1999. Ocean general circulation model sensitivity to forcing from scatterometer winds. *J. Geophys. Res.* **104**(C5): 11337–11358.

Milliff RF, Morzel J, Chelton DB, Freilich MH. 2004. Wind stress curl and wind stress divergence biases from rain effects on QSCAT surface wind retrievals. *J. Atmos. Oceanic Technol.* **21**: 1216–1231.

Nittis K, Tziavos C, Bozzano R, Cardin V, Thanos Y, Petihakis G, Schiano ME, Zanon F. 2007. The M3A multi-sensor buoy network of the Mediterranean Sea. *Ocean Sci.* **3**: 229–243.

Patoux J, Brown RA. 2001. Spectral analysis of QuikSCAT surface winds and two-dimensional turbulence. *J. Geophys. Res.* **106**(D): 23995–24005.

Pinardi N, Masetti E. 2000. Variability of the large-scale general circulation of the Mediterranean Sea from observations and modelling: A review. *Palaeo* **158**: 153–173.

Pinardi N, Robinson AR. 1987. Dynamics of deep thermocline jets in the polymode region. *J. Phys. Oceanogr.* **17**(8): 1163–1188.

Pinardi N, Allen I, Demirov E, De Mey P, Korres G, Lascaratos A, Le Traon P-Y, Maillard C, Manzella G, Tziavos C. 2003. The Mediterranean Ocean Forecasting System: First phase of implementation (1998–2001). *Ann. Geophys.* **21**: 3–20.

Pinardi N, Bonazzi A, Dobricic S, Milliff RF, Wikle CK, Berliner LM. 2011. Ocean ensemble forecasting. Part II: Mediterranean Forecast System response. *Q. J. R. Meteorol. Soc.*, DOI: 10.1002/qj.816

POEM Group. 1992. General circulation of the Eastern Mediterranean. *Earth Sci. Rev.* **32**: 285–309.

Portabella M, Stoffelen A. 2002. Characterization of residual information for SeaWinds quality control. *IEEE Trans. Geosci. Remote Sensing* **40**: 2747–2759.

Robert CP, Casella G. 2004. *Monte Carlo Statistical Methods*, 2nd edn. Springer: Berlin; 645 pp.

Royle JA, Berliner LM, Wikle CK, Milliff RF. 1998. 'A hierarchical spatial model for constructing surface winds from scatterometer data in the Labrador Sea', in *Case Studies in Bayesian Statistics IV*, C. Gatsonis, R.E. Kass, A. Cariquiry, B. Carlin, A. Cariquiry, A. Gelman, I. Verdinelli, and M. West (Eds.), Springer-Verlag: 367–381.

Ruti P, Marullo S, D'Ortenzio F, Tremant M. 2008. Comparison of analyzed and measured wind speeds in the perspective of oceanic simulations over the Mediterranean basin: QuiKSCAT and buoy data. *J. Marine Sys.* **70**: 33–48. DOI:10.1016/j.jmarsys.2007.02.026.

Song Y, Wikle CK, Anderson CJ, Lack SA. 2007. Bayesian estimation of stochastic parametrizations in a numerical weather forecasting model. *Mon. Weather Rev.* **135**: 4045–4059.

Stevens B, Duan J, McWilliams JC, Munnich M, Neelin JD. 2002. Entrainment, Rayleigh friction, and boundary layer winds over the Tropical Pacific. *J. Climate* **15**: 30–44.

Tonani M, Pinardi N, Dobricic S, Pujol I, Fratianni C. 2008. A high-resolution free-surface model for the Mediterranean Sea. *Ocean Sci.* **4**: 1–14.

Weijer W, Gille S.T. 2005. Adjustment of the southern ocean to wind forcing on synoptic time scales. *J. Phys. Oceanogr.* **35**: 2076–2089.

Wikle CK. 2003. Hierarchical models in environmental science. *Int. Statist. Rev.* **71**: 181–199.

Wikle CK, Milliff RF, Large WG. 1999. Surface wind variability on spatial scales from 1 to 1000 km observed during TOGA COARE. *J. Atmos. Sci.* **56**: 2222–2231.

Wikle CK, Milliff RF, Nychka D, Berliner LM. 2001. Spatiotemporal hierarchical Bayesian modeling: Tropical ocean surface winds. *J. Amer. Statist. Assoc.* **96**: 382–397.

